# *THEORETICAL STUDIES OF MICROFLUIDICS: "WALKING" DROPS AND "MELTING" SNOWFLAKES*


ALMA MATER STUDIORUM
UNIVERSITÀ DI BOLOGNA

Department of Chemistry "G. Ciamician"

Dr. Tommaso Gallo

Supervisor: Prof. Francesco Zerbetto

PhD coordinator: Prof. Giuliano Longoni

PhD thesis in

*"Chemical Science", Cicle XXIII*

*Scientific discipline: Physical Chemistry (CHIM/02)*

2011

# Contents

**List of Figures** iii

**List of Tables** v

**1 Introduction** 1

**2 Droplet slippage on special surfaces** 3

2.1 Experimental background . . . 3

2.2 Computational methods . . . 8

2.2.1 Computer simulations of liquids . . . 8

2.2.2 Molecular Mechanics and Force Fields . . . 8

2.2.3 Energy minimization methods . . . 12

2.2.4 Molecular Dynamics methods . . . 14

2.2.5 Steps in a MD Simulation . . . 15

2.2.6 Finite difference methods in MD simulations . . . 17

2.2.7 MD simulations at constant Temperature and Pressure . . . 19

2.2.8 Force Fields for Liquid Water . . . 21

2.2.9 The SPC water model . . . 23

2.2.10 NAMD: Scalable Molecular Dynamics . . . 25

2.3 Simulations . . . 28

2.3.1 Study systems: The drop / The surface / The drop adsorbed on the surface . . . 28

2.3.1.1 The drop . . . 28

2.3.1.2 The surface . . . 29

2.3.1.3 The drop adsorbed on the surface - different wettability 31

2.3.2 Slippage simulations . . . 32

2.3.2.1 Surface with a gradient - step-like potentials . . . . . 32
2.3.2.2 Surface with a gradient - slide-like potentials . . . . . 33
2.4 Analysis . . . . . 38
2.4.1 Slippage velocity . . . . . 38
2.4.1.1 Different mass . . . . . 38
2.4.1.2 Gap in repulsive coefficients $A_{1/2}$ . . . . . 40
2.4.1.3 Slide width $\sigma$ . . . . . 41
2.4.2 Efforts to identify elements constituting the driving force of droplet slippage . . . . . 43
2.4.2.1 Density . . . . . 44
2.4.2.2 Residence time . . . . . 47
2.4.2.3 Hydrogen bonds . . . . . 48
2.4.2.4 Diffusion coefficient . . . . . 49
2.4.2.5 Dipole orientation and dipole-dipole interaction energies 50
2.5 Final considerations about droplet slippage investigation . . . . . 52

**3 Mesoscopic study of snowflake fractals melting 53**
3.1 von Koch fractal . . . . . 53
3.2 Development of a new simulation algorithm . . . . . 54
3.2.1 Snow-fractal building . . . . . 55
3.2.2 Lattice definition . . . . . 58
3.2.3 Simulation algorithm - $MCRWS$ . . . . . 59
3.3 Ice parameter derivation . . . . . 62
3.4 Simulations . . . . . 66
3.4.1 Border length . . . . . 66
3.4.2 Radius of gyration . . . . . 67

**4 Conclusions 71**

**References 73**

# List of Figures


2.1 Photo–responsive rotaxane. . . . . 4
2.2 Photo-switchable Self–Assembled Monolayer. . . . . 5
2.3 Light-driven transport of drop slippage on functionalized glass. . . . . 6
2.4 Light-driven transport of drop slippage on functionalized mica. . . . . 7
2.5 Light-driven transport of drop on functionalized mica 12° incline. . . . . 7
2.6 Schematic of a molecular force field. . . . . 10
2.7 Water models. . . . . 22
2.8 Lennard-Jones potential for the SPC/E model (solid red line) and an equivalent Buckingham potential. . . . . 24
2.9 The SPC water molecule. . . . . 25
2.10 The two spherical cutted drops. . . . . 28
2.11 Drops after 1.5 *ps* of MD equilibration. . . . . 29
2.12 Lennard-Jones and modified for surface potentials. . . . . 30
2.13 Equilibration result for different repulsive terms. . . . . 31
2.14 Step-like potential representation. . . . . 33
2.15 Simulation snapshots of a surface adsorbed droplet under the influence of a step-like potential surface. . . . . 34
2.16 Slide-like potential representation. . . . . 35
2.17 3 *ns* Simulation snapshots on step-like potential surface. . . . . 36
2.18 1.5 *ns* Simulation snapshots on step-like potential surface of the smaller drop. . . . . 37
2.19 $y$-coordinate of the center of mass of differently sized droplets and evolution over MD simulation time. . . . . 39

## LIST OF FIGURES


2.20 $y$-coordinate of the center of mass of differently sized droplets at increased $A_{1/2}$ gap and evolution over MD simulation time. . . . . 39
2.21 $y$-coordinate of COMs of large droplets comprising 3,186 water molecules for a series of increasing $A_{1/2}$ gaps and evolution over MD simulation time. 40
2.22 $y$ coordinate of COM of a large droplet comprising 3,186 water molecules at varying slide width $\sigma$. . . . . 41
2.23 $y$ coordinate of COM of a large droplet comprising 3,186 water molecules at varying slide width $\sigma$. . . . . 42
2.24 Graphical representation of local boxes (black squares) to which property calculation is restricted. . . . . 43
2.25 Partial density analysis along the $y$-axis - 15–150 $ps$. . . . . 45
2.26 Partial density analysis along the $y$-axis - 300–450 $ps$. . . . . 45
2.27 Partial density analysis along the $y$-axis - 600–750 $ps$. . . . . 46
2.28 Residence times. . . . . 47

3.1 von Koch curve construction step. . . . . 54
3.2 Snowflake photo and von Koch fractal representation. . . . . 55
3.3 Builded filled $4^{th}$ generation von Koch snow crystal. . . . . 56
3.4 Peripheral and total amount of beads. . . . . 57
3.5 Lattice representation. . . . . 58
3.6 Lattice representation. . . . . 59
3.7 Simulation snapshots of a von Koch crystal of generation $3^{rd}$. . . . . 61
3.8 Ice crystal generated for Molecular Dynamics simulation. . . . . 62
3.9 TIP4P/Ice water model sites. . . . . 63
3.10 Evolution of filled von Koch-like structures. . . . . 64
3.11 Fit of border length of $3^{rd}$ generation von Koch fractal versus time in seconds. . . . . 65
3.12 $MCRWS$ simulation snapshot of $5^{th}$ generation snow-fractal. . . . . 67
3.13 Normalized snowflake border length. . . . . 68
3.14 Normalized border length and normalized gyration radius, versus time in arbitrary units. . . . . 70

# List of Tables


2.1 Velocities determined for various gaps in repulsive coefficients $A_{1/2}$. . . . 41

2.2 Residence times in several zones at different instances of MD simulation ($ps$) . . . . . 48

2.3 Average numbers of hydrogen-bonds formed in different zones at different instances of MD simulation. . . . . 49

2.4 Mean diffusion coefficients averaged over 150 $ps$ ($\times 10^{-9}$ $m^2/s$) . . . . . 50

2.5 Mean water dipole orientations in selected zones at different stages of droplet translocation . . . . . 51

2.6 Average dipole-dipole interaction energies in selected zones at different stages of droplet slippage ($kcal\ mol^{-1}\ molecule^{-1}$) . . . . . 51

3.1 Weights and exponential coefficients of Eq.(3.7) referred to Fig.3.13. . . 68

## LIST OF TABLES

# 1

# Introduction

In recent years, considerable progress has been made in the field of miniaturization. It is now effectively possible to miniaturize a great variety of different systems reaching from mechanical, fluidic, electromechanical and thermal devices down to nanometer-sized machines where crucial processes need to be controlled on sub-micrometer length scales. Many of these systems employ fluidic flows operating under extreme conditions difficult to explore by experimental as well as theoretical methods. The importance of the subject naturally led to the creation of a new discipline — microfluidics[1]. Microfluidics can be defined[2] as the study of flows that are simple or complex, mono- or multiphasic in nature but certainly involved in the mechanics of artificial microsystems. The latter usually refers to novel fabrication techniques[3].

The present PhD thesis summarizes two examples of research in microfluidics. Both times water was the subject of interest, once in the liquid state (droplets adsorbed on chemically functionalized surfaces), the other time in the solid state (ice snowflakes and their fractal behaviour).

The first problem deals with a slipping nano-droplet of water adsorbed on a surface with photo-switchable wettability characteristics. Main focus was on identifying the underlying driving forces and mechanical principles at the molecular level of detail. Molecular Dynamics (MD) simulation was employed as investigative tool owing to its record of successfully describing the microscopic behaviour of liquids at interfaces (see for example ref. [4] and references therein).

## 1. INTRODUCTION

To reproduce the specialized surface on which a water droplet can effectively "walk", a new implicit surface potential was developed. Applying this new method the experimentally observed droplet slippage could be reproduced successfully.

Next the movement of the droplet was analyzed at various conditions emphasizing on the behaviour of the water molecules in contact with the surface. The main objective was to identify driving forces and molecular mechanisms underlying the slippage process.

The second part of this thesis is concerned with theoretical studies of snowflake melting.

The mechanism of snow-crystal growth leading to the many different forms of snowflakes as well as the corresponding melting dynamics are both phenomena not entirely understood by today's models. The subject is interesting not only from a basic scientific point of view but has a practical component too, for example in related areas such as hydrology or climate research. Illustrative topics were for example avalanche prediction[5, 6] or dry snow scattering to mention just a few. Both of the examples seem to be connected to surface roughness, hence the study subject of this thesis.

In the present work snowflakes are represented by filled von Koch-like fractals[7] of mesoscopic beads.
A new algorithm has been developed from scratch to simulate the thermal collapse of fractal structures based on Monte Carlo and Random Walk Simulations ($MCRWS$). The developed method was applied and compared to Molecular Dynamics simulations regarding the melting of ice snowflake crystals and new parameters were derived from this comparison.

Bigger snow-fractals were then studied looking at the time evolution at different temperatures again making use of the developed $MCRWS$ method. This was accompanied by an in-depth analysis of fractal properties (border length and gyration radius) in order to shed light on the dynamics of the melting process.

# 2

# Droplet slippage on special surfaces

## 2.1 Experimental background

Specialized surfaces coated with stimuli-responsive rotaxanes have been suggested by *P. Rudolf et al. (2005)*[8] as molecular switches to trigger the slippage of a liquid drop. Such rotaxanes capable of working as a wettability switch are stimuli-responsive molecular shuttles in which the mobile element — the macrocycle — is translocated from one position ("station") of the thread (the static element) to the other position of the thread (at the opposite end) via biased Brownian motion.
This movement is in response to an external signal (for example, light, electrons, temperature, pH, nature of the environment, reversible covalent bond formation, and so on)[9, 10, 11, 12, 13, 14, 15, 16, 17, 18, 19].

These systems are viewed as potential elements for molecular machinery and the change in position of the subunits has been used as a nanoscale mechanical switch to vary physical properties such as conductivity[13], induced circular dichroism[14] and fluorescence[15, 16, 17, 18].

In applying a system of the type shown in figure 2.1 Rudolf et al. speculated on a stimuli-induced co-conformational change: the photoisomerization[19] of the fumaramide station (which has a high binding affinity for the ring) to maleamide (which has a low binding affinity for the ring) induce the macrocycle to conceal a short fluoroalkane segment (the tetrafluorosuccinamide station).

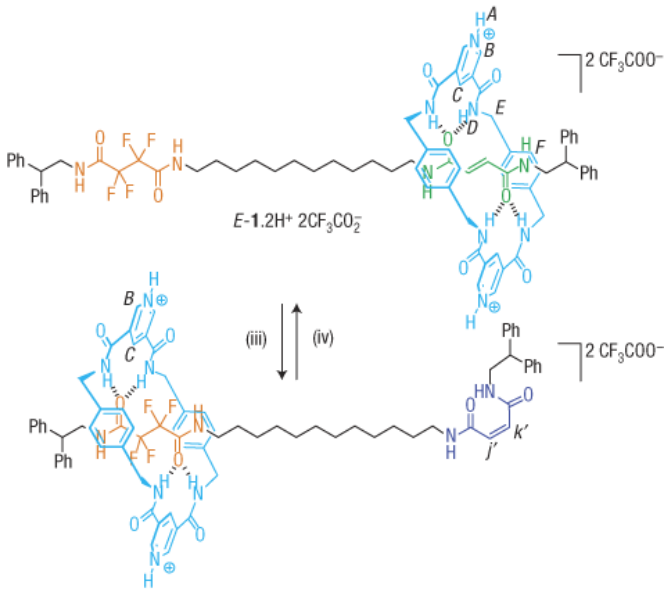


**Figure 2.1: Photo–responsive rotaxane.**

Contact angles[20] of liquid droplets are commonly used to describe the tendency of a liquid to "wet" a solid surface [21].

Since contact angles of both polar as well as apolar liquids show considerable dependence on even small amounts of fluoroalkane[22], they appear to provide a convenient means to characterize the photo-switchable wettability system of Rudolf et al. So, the shuttling effect described before was used to produce a rotaxane-terminated surface with photo-switchable wettability characteristics[23] (see figure 2.2).

Indeed, small (0.5–5 $\mu l$) droplets of several low-volatility liquids (for example, water, formamide ($H_2NCHO$), ethylene glycol and diiodomethane ($CH_2I_2$)) was deposited on rotaxane-terminated surfaces; each of them showed significantly (8–22°) lower contact angles after irradiation for 5 min with ultraviolet light[24, 25, 26, 27, 28, 29].

A 1.25 $\mu l$ drop of diiodomethane, the liquid that showing greatest discrimination between the pristine and irradiated surfaces, was deposited on functionalized glass and irradiated with a perpendicular beam of 240–400 nm light focused on one side of the drop and the adjacent area in order to produce a gradient in the surface free energy across the length of the drop (figure 2.3a).

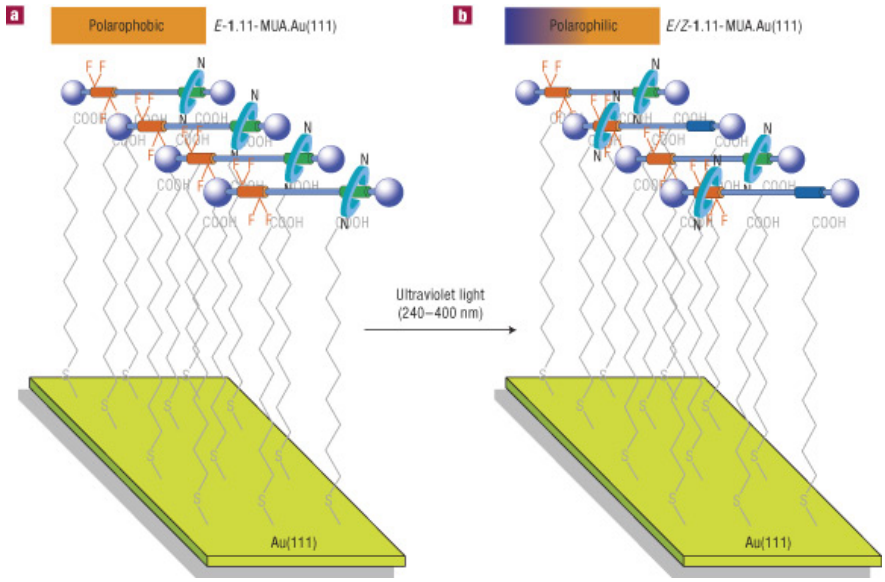


**Figure 2.2: Photo-switchable Self–Assembled Monolayer.**

The irradiation caused the reduction of the front of the drop contact angle and its start of advance in direction of the polarophylic side (figure 2.3b). The advancing contact angle remained lower than the receding contact angle during this initial extension period, the inequality of contact angles illustrating the difference in surface properties caused by the irradiation.
This initial period was followed by a subsequent phase of steady transport during which the entire droplet moved at a mean speed of $\sim 1\mu m/s$ and contact angles on the illuminated and non-illuminated side remained essentially equivalent (figure 2.3c).
The drop eventually stops after having traversed a distance of $\sim 1\ mm$ (figure 2.3d).

Mica provides a flatter and more regular surface than glass and consequently self-assembled monolayers (SAM) are generally more ordered using Au(111) deposited on mica. Although the contact angles were the same for the SAMs on the different substrates the transport of $CH_2I_2$ was significantly more efficient using mica. Indeed, the rear end of the droplet could be transported more than 1.5 $mm$ on such a different type of photo-responsive surface (figure 2.4).

A final experiment was concerned with the potential of photo-responsive molecular switches to do macroscopic work against gravity. Here the goal was to make use of

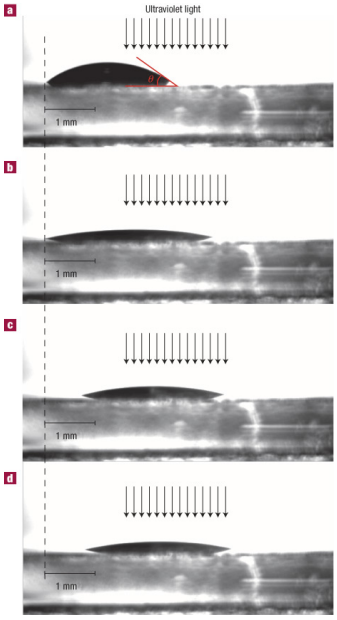


**Figure 2.3: Light-driven transport of drop slippage on functionalized glass.**

the aforementioned principle and enforce an "uphill movement" of a small droplet. In fact, the authors could show that at the same experimental conditions described in the previous scenario, a small droplet could be driven up a 12° incline using functionalized mica (figure 2.5)[30].

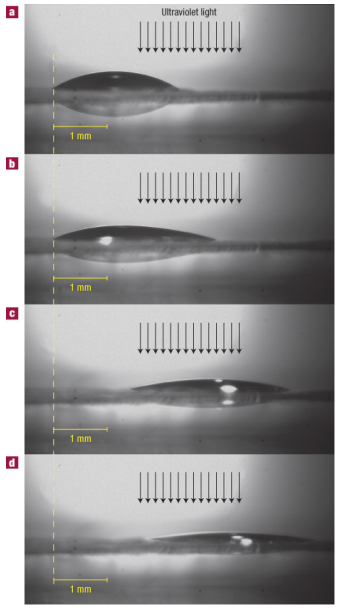


**Figure 2.4: Light-driven transport of drop slippage on functionalized mica.**

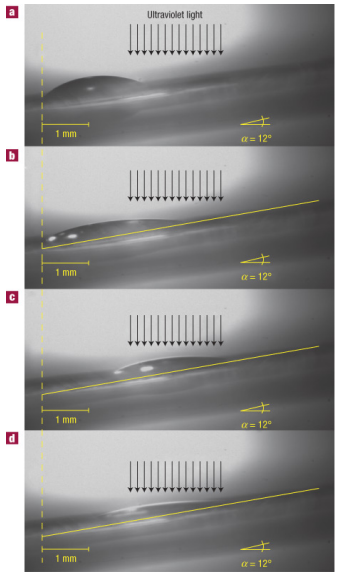


**Figure 2.5: Light-driven transport of drop on functionalized mica 12° incline.**

## 2.2 Computational methods

In this section the theoretical and computational basis of the methods used in this PdD project. The fundamental theory that is behind Molecular Mechanics and Molecular Dynamics is reported together with the most important mathematical algorithm methods used. A brief excursus on the main theoretical models developed to describe liquid water is presented.

### 2.2.1 Computer simulations of liquids

Molecular Dynamics (MD) simulations permit the study of complex systems, i.e. the systems containing a lot of interacting particles.

Liquids represent the state of matter most frequently studied by MD methods. This is due to historical reasons, since both solids and gases have well-developed theoretical foundations, but there is no general theory of liquids. For solids, theory begins by assuming that the atomic constituents undergo small oscillations about fixed lattice positions; for gases, independent atoms are assumed and interactions are introduced as weak perturbations. In the case of liquids, however, the interactions are as important as in the solid state, but there is no underlying ordered structure to begin with. It is now over 35 years since the first computer simulation of a liquid was carried out at the Los Alamos National Laboratories in the United States on a super-computer called MANIAC. Rapid development of computer technology makes now possible to perform long simulation with many particles. After an initial groundwork on atomic systems, computer simulation developed rapidly[31].

Due to its ubiquity in our environment, water still remains one of the most interesting liquid to study and so far a lot of theoretical models were developed in order to describe the experimental properties of this liquid.

### 2.2.2 Molecular Mechanics and Force Fields

The microscopic state of a molecular system can be described by defining the position ($q_i$) and momentum ($p_i$) of each particle of the system at every time.
Considering the Born-Oppenheimer approximation, the Hamiltonian of a system can be expressed as a function of the nuclear variables, the rapid motion of the electrons having been averaged out. This classical approach requires the use of Force Field (from

now on, $FF$) methods, known as Molecular Mechanics ($MM$), which consider the total potential energy of a chemical structure as a fun[21]ction of the only nuclear atomic positions. Making the additional approximation that a classical description is adequate, we may write the Hamiltonian $H$ of a system containing $N$ particles as a sum of kinetic and potential energy:

$$H(q^N, p^N) = K(p^N) + V(q^N) \tag{2.1}$$

Usually the kinetic energy K takes the form

$$K = \sum_{i=0}^{N} \sum_{\alpha} \frac{p_{i\alpha}^2}{2m_i} \tag{2.2}$$

where $m_i$ is the molecular mass and the index runs over the different $(x, y, z)$ components of the momentum of the molecule $i$.

The potential energy $V$ may be divided into terms depending on the coordinates of individual atoms for the given conformation, such as the stretching of bonds, the opening and closing of angles, the rotation about single bonds and the long range interactions. It can be expressed as follows:

$$\begin{aligned} V(q^N) \quad = \quad & \sum_{bonds} \frac{k_i}{2}(l_i - l_{i,0})^2 + \sum_{angles} \frac{k_i}{2}(\theta_i - \theta_{i,0})^2 + \\ & \sum_{torsions} \frac{V_N}{2}\left[1 + cos(n\omega - \gamma)\right] + \\ & \sum_{i=1}^{N} \sum_{j>1}^{N} \left\{ 4\varepsilon_{ij} \left[ (\frac{\sigma_{ij}}{r_{ij}})^{12} - (\frac{\sigma_{ij}}{r_{ij}})^{6} \right] + \frac{Q_i Q_j}{4\pi\varepsilon_0 r_{ij}} \right\} \end{aligned} \tag{2.3}$$

Equation 2.3 represents the simplest MM Force Field.

As it is shown in Figure 2.6, the mechanical molecular model considers atoms as spheres and bonds as springs.

The mathematics of spring deformation can be used to describe the ability of bonds to stretch, bend, and twist. In fact, the first term of the potential energy function in equation 2.3 is similar to the Hookes law for a spring deformation. It represents the

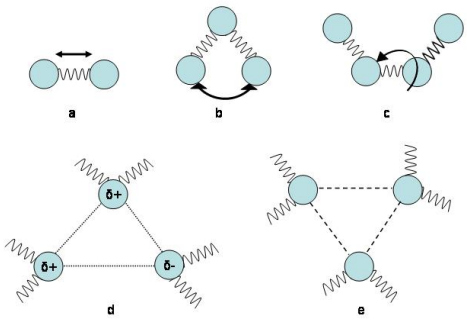


**Figure 2.6: Schematic of a molecular force field.** The mechanical molecular model considers atoms as spheres and bonds as springs. The mathematics of spring deformation can be used to describe the ability of bonds to stretch (a), bend (b), and twist (c). Non-bonded atoms (greater than two bonds apart) interact through van der Waals attraction, steric repulsion, and electrostatic attraction/repulsion. These properties are easiest to describe mathematically when atoms are considered as spheres of characteristic radii (d,e).

bond stretching and describes the interaction between pairs of bonded atoms by a harmonic potential, increasing in energy as the bond length $l_i$ deviates from its reference value $l_{i,0}$. The second term is the angle of bending $\theta_i$ of the molecule, again modelled using a harmonic potential. In both terms, $k_i$ represents the forces constant. The third term is a torsional potential that shows how the energy changes as a bond rotates: the $V_n$ parameter controls the amplitude of the curve, the n parameter controls its periodicity and reflects the type symmetry in the dihedral angle, and $\gamma$ shifts the entire curve along the rotation angle axis $\omega$.

Non-bonded atoms (greater than two bonds apart) interact through van der Waals attraction, steric repulsion, and electrostatic attraction/repulsion. These properties are easiest to describe mathematically when atoms are considered as spheres of characteristic radii. Therefore the fourth contribution is the non-bonded term, calculated between all pairs of atoms belonging to different molecules or to the same molecule but separated by at least three bonds. In a simple $FF$, the non-bonded term is usually modelled using a Coulomb potential term for electrostatic interactions, where $Q$ are the charges and $r_{ij}$ the distances, and a Lennard-Jones or Buckingham potential for Van der Waals

interactions, where $\varepsilon_{ij}$ and $\sigma_{ij}$ control the depth and position (interatomic distance) of the potential energy well for a given pair of non-bonded interacting atoms. The $FF$, thus, enables the potential energy of a molecule (or of a system of molecules) to be calculated rapidly and pretty accurately. It also allows describing the energy changes of the molecule caused by internal system changes, like rotations around a bond, as well as the interactions between non-bonded parts of the system. More sophisticated $FF$ may have additional terms, but they contain the same four fundamental components. Few important features characterize a Molecular Mechanics Force Field:

- *The parameter set implemented in the functional form.* Parameters quantitatively define the single energy contributions for each group of interacting atoms and, as a consequence, they govern the computation of the whole energy function.
- *Transferability of parameters.* The same set of parameters can be used to model a series of related molecules, not explicitly included during the parameter optimisation, rather than having to define a new set of parameters for each individual molecule. Transferability has some limitations: the larger the number of parameters that are extrapolated, the lower the accuracy of the force field.
- *The empirical form.* There is not an "a priori" form for a FF. The functions of a FF very often are meant to offer a compromise between accuracy and computational efficiency: the most accurate functional form may often be unsatisfactory for efficient computation.
- *The Atom Type concept.* It is more that the simple atomic number. It contains information about the hybridization state (i.e. an implicit description of the motion of its electrons) and, sometimes, about the local environment of an atom. When preparing an input for MM it is necessary to assign an atom type for each atom in the system.

The parameterization of the $FF$ represents the most difficult and time-consuming step in a $MM$ calculation. Once the right functional form for describing the system has been chosen, one has to decide which set of parameters to introduce. Derived parameters are expected to be transferable to other classes of molecules. Transferability is one of the most important properties of a force field.

### 2.2.3 Energy minimization methods

The most popular application of the empirical potential energy function is to find the geometry of a molecule (or an assemblage of molecules) which corresponds to a minimum of the potential energy function. In MM, the energy of a molecule in its ground electronic state is a function of only the coordinates of its atoms. If nuclei move, the energy changes. Such changes in energy can be considered as displacements on a multidimensional surface, called the Potential Energy Surface (PES).

The minimization of the potential energy function (i.e., geometry optimization) involves a search for the minimum of a function and usually requires calculations of derivatives of the potential energy function versus independent variables (in our case, coordinates). Most programs use cartesian coordinates as independent variables, however, in some cases, internal coordinates may be used. The derivatives of potential energy are denoted as:

$$g_i = \frac{\partial V}{\partial x_i}; \qquad H_{ij} = \frac{\partial^2 V}{\partial x_i \partial x_j} \tag{2.4}$$

where $g_i$ is the gradient (i.e., first derivative) of the potential energy $V$ with respect to a cartesian coordinate $x_i$ of an atom; $_{ij}$, called Hessian matrix, is the second derivative of the energy with respect to the cartesian coordinates. In most modern programs these derivatives are calculated analytically, i.e., the appropriate mathematical formulae for corresponding terms are incorporated into the program. Some older codes compute derivatives numerically by approximating the slope of an energy function (or its gradient in the case of second derivatives) from finite differences. The derivatives are used not only in function minimization but also yield forces acting on atoms (from energy gradients) and normal modes of vibration (from the Hessian matrix).

There are three major approaches to find a minimum of a function of many variables:

- **Search Methods:** utilize only values of the function itself. They are usually slow and inefficient, but are very simple to program, since deriving cumbersome formulas for derivatives is not necessary. In spite of their inefficiency, the search algorithms are infallible and always find a minimum. For this reason, they are often used as an initial step, when the starting point in optimization is far from the minimum. Another disadvantage of search techniques is that they are very

inefficient for a large number of optimized variables and converge very slowly when the number of variables is more then 10.

- **Gradient Methods:** utilize values of a function and its gradients. These are currently the most popular methods in molecular mechanics. They offer a much better convergence rate than search methods and do not require a lot of computer memory (only $3N$ first derivatives are needed). However, in some situations they fail to converge to a minimum. The *conjugated gradient* algorithm is considered the most robust in this class.
- **Newton Methods:** are the most rapidly converging algorithms which require values of function, and its first and second derivatives. The memory required for storing the Hessian matrix is proportional to $N^2$ (i.e., prohibitive for large macromolecules). The BFGS algorithm is considered the most refined one.

In general, the minimization methods are iterative. They require on input some initial estimate for the position of the minimum, and provide a better estimate for the minimum as a result. This corrected estimate is used as an input into the next cycle (i.e. iteration) and the process is continued until there is no significant improvement in the position of the minimum.

Most search methods and minimization methods using derivatives are the *descent series methods*, i.e., each iteration results in a solution which corresponds to a lower (or equal) value for the energy function:

$$V(x^{(start)}) \geq V(x^{(1)}) \geq V(x^{(1)}) ... \geq V(x^{(min)}) \tag{2.5}$$

As a consequence, these methods can only find the minimum closest to the starting estimate and will never cross to a minimum (however deep) if it is separated from the starting estimate by a maximum (however small). There is no general way of finding a global minimum (i.e., the minimum corresponding to the lowest possible value of the function). A different initial geometry will usually lead to a different final minimum.

Only on very simple molecules will the single geometry optimization yield the global minimum on the first trial. To find a global minimum one has to perform many minimizations and use different initial coordinates for each run[32].

### 2.2.4 Molecular Dynamics methods

Computer simulation methods allow the analysis of complex systems, by producing replications of the macroscopic system with a handy and manageable number of particles. A computer simulation generates a representative ensemble of possible configurations of these small replications: in this way accurate calculations of structural and thermodynamic properties can be performed, by analysing the mechanical properties of molecules. Therefore the behaviour of the system in time can be studied and properties such as internal energy, entropy, pressure, temperature and so on, can be determined.

Among all the different kinds of computer simulation methods available, Molecular Dynamics ($MD$) simulations were performed during my PhD project to study the dynamical evolution of collapsing bubble.

MD simulations address numerical solutions of Newtons equations of motion on an atomistic or similar model of a molecular system. In fact, all of the information needed to calculate the dynamics of a system can be found from the potential energy function $V$ of the system.

The force $F$ on atom $i$ in the system can then be determined from the equation:

$$F_i = -\nabla_i V \tag{2.6}$$

Using the Newton classical approximation, MD simulates the motion of particles in a system they react to forces caused by interactions with other particles. Forces so evaluated are used to determine accelerations. Particle velocities are initially determined by a random distribution, but then they are updated according to the calculated accelerations.

For the continuous nature of the potential functions describing interactions between atoms or molecules, it is necessary to integrate the equations of motion by dividing the calculation into a series of short time steps, which should be at least one order of magnitude shorter than the shortest motion simulated. An important assumption to be made is to consider forces acting on the atoms constant over the time-interval: at each step forces are recomputed and a new set of accelerations, velocities and positions

are obtained. Following this technique, MD simulations generate a trajectory of the system describing its evolution over time.

The general property $A$ of the system is calculated as an average upon all the $M$ visited states:

$$\langle A \rangle = \frac{1}{M} \sum_{i=1}^{M} A_i(q^N, p^N) \tag{2.7}$$

where $q$ refers to the coordinates and $p$ to the linear momenta of the $N$ particles constituting the system.

MD simulations can thus be considered as a deterministic method: they provide information about the "real" evolution of the system over time, and they allow to go back over past states of the system as well as to predict future arrangement of its particles. This dynamical view of molecular systems thus provides a useful and important tool for studying time-dependent processes.

### 2.2.5 Steps in a MD Simulation

The first thing before starting with a MD simulation is to decide which FF to use to model the interactions between atoms or molecules in the system.
A simulation can then be described according to four principal points:

- **Choice of the initial configuration.** This is a crucial moment of the entire simulation. Its very important to set up starting configuration of the system as much as possible similar to the real conformation; in fact, wrong starting coordinates may compromise the whole simulation process. Generally, homogeneous liquids (i.e., composed by molecules of the same type) are described by a standard lattice structure (for example, a face-centred cubic lattice) as starting configuration. The dimensions of the lattice are chosen in such a way to respect as much as possible the real density of the simulated systems. Usually, before proceeding with the simulation, a first minimization of the system energy is required in order to eliminate any term of high energy, which may cause instability in the simulation.

- **Equilibration phase.** The system is allowed to evolve from the initial configuration until certain stability in the simulation is reached. At this stage, thermodynamic and structural properties, such as energy, temperature, pressure, are monitored: once their values have become stable, equilibration is reached. Order parameters can be also used to check when an equilibration phase can be considered completed.
- **Production phase.** This is the real simulation stage. The system is set free to evolve and it is possible to calculate reliable properties.
- **Analysis.** Properties not calculated during the simulation from the molecular mechanics program are evaluated and the configurations produced (and stored) are examined. This phase is important not only to know how the system changes, but also to check if any problems occurred during the simulation after the equilibration step.

When starting an MD simulation, the initial velocities of all the molecules must be specified: this usually is done by randomly selecting a set of velocities from the Maxwell-Boltzmanns distribution at the temperature of the simulation.

$$p(v_{ix} = \left(\frac{m_i}{2\pi k_B T}\right)^{1/2} \exp\left(\frac{-\frac{1}{2}m_i v_{ix}^2}{k_B T}\right) \tag{2.8}$$

The Gaussian distribution of Equation 2.8 gives the probability $p(v_{ix})$ that an atom $i$ of mass $m_i$, has a velocity $v_{ix}$ in the $x$ direction at the temperature $T$. Initial velocities are usually adjusted to give a zero total linear momentum:

$$P = \sum_{i=1}^{N} m_i v_i = 0 \tag{2.9}$$

The normal process of equilibration will then redistribute the energy amongst the different degrees of freedom. Precise adjustments to the kinetic temperature are made by scaling velocities during equilibration.

Careful monitoring of the behaviour of properties during the simulation can help to check if problems occur, and in this unfortunately case, the simulation has to be restarted from scratch after removing the cause of the problem.

### 2.2.6 Finite difference methods in MD simulations

Finite difference methods are the numerical recipes used in $MD$ simulations to integrate equations of motion and to generate trajectories, under the assumption that the energy potential terms are pair wise additive. If we consider a system of atoms, with Cartesian coordinates ri and the usual definition of $K$ (Eq. 2.2) and V (Eq. 2.3) then the equation of motion becomes:

$$m_i \ddot{r}_i = F_i \tag{2.10}$$

where $m_i$ is the mass of atom $i$ and $F_i$ is defined by Equation 2.6.

For a given FF characterizing the physical system, the integration method is responsible for the accuracy of the simulation results. If the integration method works correctly, the simulation will provide exact results, within the errors due to the computer finite number representation. However, any finite difference method is naturally an approximation for a system evolving continuously in time. An integration algorithm or integrator is required to have some well defined features such as:

- *Accuracy.* It has to approximate the true trajectory.
- *Stability.* It has to avoid small perturbations generating numerical instabilities.
- *Robustness.* It should allow integrations for relatively long time steps.

A standard method for solution of ordinary differential equations is the finite difference approach. Given the molecular positions, velocities, and other dynamic information at time $t$, we attempt to obtain the positions, velocities etc. at a later time $t + \delta t$. The equations are solved on a step-by-step basis; the choice of the time interval $\delta t$ will depend somewhat on the method of solution, but $\delta t$ will be significantly smaller than the typical time taken for a molecule to travel its own length.

The simplest and most straightforward way to construct an integrator is by expanding positions and velocities in Taylor series. Dividing the simulation in fixed time intervals, $\delta t$, the expansion reads:

$$r(t + \delta t) = r(t) + v(t)\delta t + \frac{1}{2}a(t)\delta t^2 + \frac{1}{6}b(t)\delta t^3 + \dots \tag{2.11}$$

$$v(t + \delta t) = v(t) + a(t)\delta t + \frac{1}{2}b(t)\delta t^2 + \dots \tag{2.12}$$

$$a(t+\delta t) = a(t) + b(t)\delta t \tag{2.13}$$

where $v$ is the velocity, $a$ the acceleration, and $b$ the third derivate, and so on.

The Verlet algorithm[33] is probably the most used method for integrating the equations of motion in MD simulation. This method uses the positions and the accelerations at the time $t$, and the positions from the previous step, $r(t-\delta t)$, to calculate the new positions at $t+\delta t$. The Verlet algorithm equations are written in the following way:

$$r(t+\delta t) = r(t) + v(t)\delta t + \frac{1}{2}a(t)\delta t^2 + \ldots \tag{2.14}$$

$$r(t-\delta t) = r(t) - v(t)\delta t + \frac{1}{2}a(t)\delta t^2 + \ldots \tag{2.15}$$

By adding the two last equations one obtains:

$$r(t+\delta t) = 2r(t) - r(t-\delta t) = r(t)a(t)\delta t^2 \tag{2.16}$$

In the Verlet integration algorithm velocities do not appear explicitly, but they can be calculated in several ways. One of these is the following:

$$v(t) = \left[r(t+\delta t) - r(t-\delta t)\right]/2\delta t \tag{2.17}$$

Implementation of the Verlet algorithm is straightforward and the storage requirements are modest and include two sets of positions ($r(t)$ and $r(t-\delta t)$) and the accelerations, $a(t)$. One of its drawbacks is that positions $r(t+\delta t)$ are obtained by adding a small term, $a(t)\delta t^2$, to the difference of two much larger terms (see Eq. 2.16). This may cause a loss of precision. The Verlet algorithm shows other problems, like the difficulty to calculate the velocities, which are not available until the positions have been computed at the next step. In addition, it is not self-starting: the new positions are obtained from the current positions $r(t)$ and the positions from the previous step, $r(t-\delta t)$. At t = 0, there is only one set of coordinates and it is necessary to employ some other ways to obtain positions at time, $t\delta t$.

A large number of variations of the Verlet algorithm have been developed:

- *The velocity Verlet* method[34] evaluates positions, velocities and accelerations at the same time and this does not affect negatively the precision of the calculation:

$$r(t+\delta t) = r(t) + v(t)\delta t + \frac{1}{2}a(t)\delta t^2 \tag{2.18}$$

$$v(t+\delta t) = v(t) - \frac{1}{2}\left[a(t) + a(t+\delta t)\right]\delta t \tag{2.19}$$

  The velocity Verlet algorithm is actually implemented as a three-stage procedure, the new velocities requiring accelerations at the times $t$ and $t+\delta t$. Thus, as first step, positions at the time $t+\delta t$ are calculated, using velocities and accelerations at time $t$, and then, velocities at time $t+\frac{1}{2}\delta t$ are determined, using the equation:

$$v(t+\frac{1}{2}\delta t) = v(t) - \frac{1}{2}a(t)\delta t \tag{2.20}$$

  The new forces are then computed from the current positions, thus giving $a(t+\delta t)$. In the final step, the velocities at time $t+\delta t$ are calculated using the following relation:

$$v(t+\delta t) = v\left(t+\frac{1}{2}\delta t\right) + \frac{1}{2}a(t+\delta t)\delta t \tag{2.21}$$

- The *Beemans* algorithm[35] uses a more accurate expression for the velocities, and, as a consequence, gives a better energy conservation and the kinetic energy can be calculated directly from the velocities:

$$r(t+\delta t) = r(t) + v(t)\delta t + \frac{2}{3}a(t)\delta t^2 - \frac{1}{6}a(t-\delta t)\delta t^2 \tag{2.22}$$

$$v(t+\delta t) = v(t) + \frac{1}{3}a(t)\delta t + \frac{5}{6}a(t)\delta t - \frac{1}{6}a(t-\delta t)\delta t^2 \tag{2.23}$$

All these methods have similar accuracies and are expected to produce identical trajectories in coordinate space.

### 2.2.7 MD simulations at constant Temperature and Pressure

Molecular dynamics simulations can be performed sampling the phase space of the system considered in ensembles: the most frequently used are the $NVE$ or *micro-canonical* ensemble, the $NVT$ or *canonical* ensemble, the $NPT$ or *isothermal-isobaric* ensemble, and the VT or grand canonical ensemble[31].

The need to maintain the temperature constant during a simulation arises from different reasons. For example, one may wish to know how a system behaves under certain temperature conditions, such as for the unfolding of protein, or in a phase transition or, also, if an annealing process has to be simulated. Moreover, it is worthwhile remembering that the temperature can be considered as an external stimulus affecting the macroscopic behaviour of a given system.
Being the temperature of the system closely related to the time average of the kinetic energy, it can be left unchanged by scaling the velocities[36] of the particles, with a multiplying factor $\lambda$, or by coupling the simulated system to an external bath[37] with a constant temperature. In the first case, the relative temperature change is given by the following equations:

$$\Delta T = \frac{1}{2}\sum_{i=1}^{N}\frac{2}{3}\frac{m_i(\lambda v_i)^2}{Nk_b} - \frac{1}{2}\sum_{i=1}^{N}\frac{2}{3}\frac{m_i v_i^2}{Nk_b} \tag{2.24}$$

$$\Delta T = (\lambda^2 - 1)\, T(t) \tag{2.25}$$

$$\lambda = \sqrt{T_{new}/T(t)} \tag{2.26}$$

In the second treatment, the bath acts as a source of thermal energy, adding or removing heat from the system introducing the possibility to change atomic velocities at each step. The rate of change of temperature is proportional to the difference in temperature between the bath and the system:

$$\frac{d(T)}{dt} = \frac{1}{\tau}\left(T_{bath} - T(t)\right) \tag{2.27}$$

The scaling factor for the velocities reads:

$$\lambda^2 = 1 + \frac{\delta t}{\tau}\left(\frac{T_{bath}}{T(t)} - 1\right) \tag{2.28}$$

If $\tau$ is large, then the coupling is weak. If $\tau$ is small, the coupling is strong. When the coupling parameter equals the time step, the algorithm becomes equivalent to the simple velocity scaling method.

In the same way, one may wish to keep the pressure constant during a simulation: this enables the study of certain phenomena such as the onset of pressure induced

phase transitions. Many methods used for pressure control are similar to those used for temperature: the pressure is maintained constant by simply scaling the volume, or by coupling the system to an external pressure bath. The rate of the pressure change is given by:

$$\frac{d(P)}{dt} = \frac{1}{\tau_P}(P_{bath} - P(t)) \tag{2.29}$$

$\tau_P$ is the coupling constant, $P_{bath}$ is the pressure of the bath, and $P(t)$ is the actual pressure at time $t$. Introducing the system compressibility, $k$, the volume of the simulation box is scaled by a factor $\lambda$, equivalent to scaling the positions by $\lambda^{1/3}$. Thus:

$$\lambda = 1 - k\frac{\delta t}{\tau_P}(P - P_{bath}) \tag{2.30}$$

$$r_i' = \lambda^{1/3} r_i \tag{2.31}$$

### 2.2.8 Force Fields for Liquid Water

In comparison with all inorganic substances having similar molecular sizes, water exhibits a remarkable set of "anomalous" physical properties that have played a primary role in the formation of a natural environment suitable for the development and maintenance of life.

Many FF for molecular simulations of liquid water have been developed over the past years in order to describe the structure of water, on the basis that if the (known) model can successfully predict the physical properties of liquid water then the (unknown) structure of liquid water is determined[38, 39].

The most popular potential models of intermolecular interactions keep the geometry of water monomer fixed with the charge distribution represented by three or four point charges equal to fractions of an electron charge. They also involve orienting electrostatic effects as Lennard-Jones sites that may or may not coincide with one or more of the charged sites (see figure 2.7). The Lennard-Jones interaction accounts for the size of the molecules. It is repulsive at short distances, ensuring that the structure does not completely collapse due to the electrostatic interactions. At intermediate distances it is significantly attractive but non-directional and competes with the directional attractive electrostatic interactions. This competition ensures a tension between an expanded

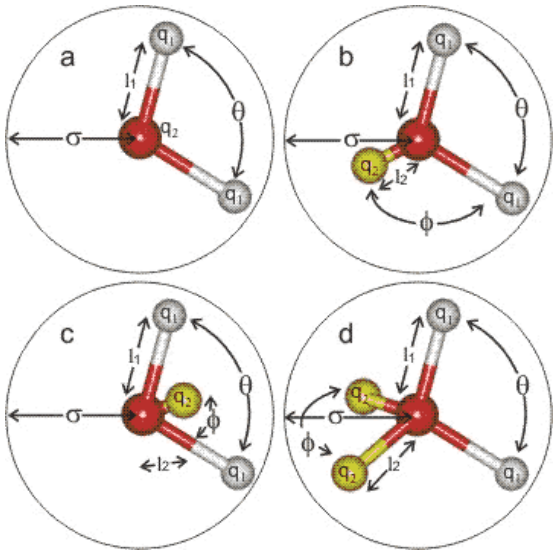


**Figure 2.7: Water models.** Models type a, b and c are all planar whereas type d is almost tetrahedral.

tetrahedral network and a collapsed non directional one (e.g. similar to that found in liquid noble gases)[40].

Generally each model is developed to fit well with one particular physical structure or parameter (e.g. the density, radial distribution function). Also, there is still disagreement over which value of some physical parameters to use, e.g. for the dipole moment. Whether model results agree with other physical properties of water then acts as proof (or otherwise) of their utility. The more fitting parameters that are required by the model (and some require over 50), the better the fit. Some models show a lack of robustness due to their sensitivity to the precise model parameters, the system size or the calculation method.

A recent review listed 46 distinct models[41], so indirectly indicating their lack of success in quantitatively reproducing the properties of real water. They may, however, offer useful insight into water's behaviour. Although such simple models are of great utility, no universally applicable model can be identified at this time. It should also be noted that many simulations are performed with just a few hundred water molecules within rectangular periodic boxes no more than 2.5 $nm$ along each edge for times

equivalent to a few picoseconds; conditions that reduce discovery of long-range effects and introduce artefacts. Use of cut-off lengths (even long ones) in the intermolecular interactions may also introduce artefacts. It should be noted that there is a strong correlation between the length scale of any water structuring and the time scale which is required to see it.

Note, however that water is not a spherically symmetrical molecule as judged by the variation in the van der Waals radii. Also, in these models the Lennard-Jones interaction exerts a repulsive effect on hydrogen bonding whereas some report it is attractive even at this close contact. The Lennard-Jones potential is made up of a twelfth power repulsive term and a sixth power attractive term:

$$V_r^{LJ} = 4\epsilon \left[ \left( \frac{\sigma}{r_{ij}} \right)^1 2 - \left( \frac{\sigma}{r_{ij}} \right)^6 \right] \tag{2.32}$$

Shown below in Figure 2.8 is the Lennard-Jones potential for the SPC/E model (solid red line). The $\sigma$ parameter gives the molecular separation for zero interaction energy. The minimum energy ($-\epsilon$) lies 12% further at $\sigma \times 2^{1/6}$ Å. Also shown (dotted blue line) is an equivalent Buckingham potential ($\sigma = 3.55$ Å, $\epsilon = 0.65\, kJ\, mol^{-1}$, $\gamma = 12.75$); the $\sigma$ parameter in the Buckingham potential gives the $\sigma \times 2^{1/6}$ position in the Lennard-Jones potential.

$$V_r^{Buckingham} = \frac{\epsilon}{1 - 6/\gamma} \left( \frac{6}{\gamma} \exp\left[ \gamma \left( 1 - \frac{r_{ij}}{\sigma} \right) \right] - \left( \frac{\sigma}{r_{ij}} \right)^6 \right) \tag{2.33}$$

Models may be checked for agreement with gas phase clusters (e.g. water dimers) before use in liquid water simulations. Such compliance, however, should not be a necessary prerequisite for accurate liquid water predictions.

### 2.2.9 The SPC water model

In this project, the SPC (Simple Point Charge) model[42, 43] for water was chosen, because despite its simplicity, it is reasonably successful to perform liquid water simulations.

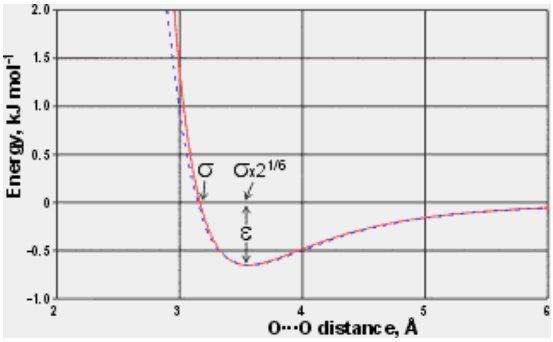


**Figure 2.8: Lennard-Jones potential for the SPC/E model (solid red line) and an equivalent Buckingham potential.**

The SPC model consists of a tetrahedral water molecule (figure 2.9) with an O–H distance of 0.1 $nm$, with three centres of concentrated charge: a predominance of positive charge on the H atoms ($q_H = +0.41\,e$) and excess negative charge on the O atom ($q_O = -0.82\,e$), and a Lennard-Jones interaction on the oxygen position, given by

$$V_{LJ}(r) = \left(\frac{A}{r}\right)^{12} - \left(\frac{B}{r}\right)^{6} \tag{2.34}$$

where $A = 0.3428\,(kJ/mol)^{1/12}nm$ and $B = 0.37122\,(kJ/mol)^{1/6}nm$.

The assumption that there are point charges is an approximation that leads to an incorrect value for the permanent dipole moment of the water. To correct this, the H–O–H bond angle is changed to 109.47° in the model (compared with the experimentally found H–O–H bond angle of 104.5°).The results of the charge concentration and the widened V-shape bond angle is that the permanent dipole moment of the SPC model water molecule has a value close to that measured in experiment. It has also an effect on the mobility of the molecule. The molecule is able to move faster than it would in "real" water due to the missing two lone electron pairs in the SPC model. This effect however decreases when the temperature is increased.
The dipole moment of the SPC model is 2.27 D, compared to 1.85 D for the isolated molecule. The diffusion coefficient of the model is $3.6\times10^{-5}\ cm^2s^{-1}$ at 300 K, compared to the experimental value of $2.4 \times 10^{-5}$.

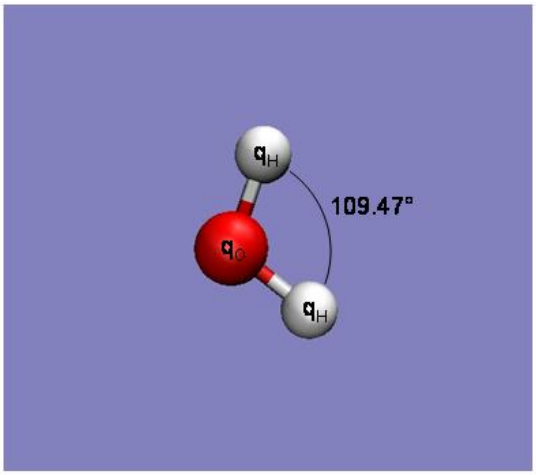


**Figure 2.9: The SPC water molecule.**

### 2.2.10 NAMD: Scalable Molecular Dynamics

In order to conduct MD simulations, various computer programs have been developed, originally developed for serial machines. Simulation of large molecular systems, however, require enormous computing power. One way to achieve such simulations is to utilize parallel computers. In recent years, distributed memory parallel computers have been offering cost-effective computational power. NAMD[44] was designed to run efficiently on such parallel machines for simulating large molecules.

NAMD has several important features:

- **Force Field Compatibility.** The force field used by NAMD is the same as that used by the programs CHARMM[45] and X-PLOR[46]. This force field includes local interaction terms consisting of bonded interactions between 2, 3, and 4 atoms and pairwise interactions including electrostatic and van der Waals forces. This commonality allows simulations to migrate between these three programs.
- **Multiple Time Stepping.** The velocity Verlet integration method[31] is used to advance the positions and velocities of the atoms in time. To further reduce the cost of the evaluation of long-range electrostatic forces, a multiple time step

scheme is employed. The local interactions (bonded, van der Waals and electrostatic interactions within a specified distance) are calculated at each time step. The longer range interactions (electrostatic interactions beyond the specified distance) are only computed less often. This amortizes the cost of computing the electrostatic forces over several timesteps. A smooth splitting function is used to separate a quickly varying short-range portion of the electrostatic interaction from a more slowly varying long-range component. It is also possible to employ an intermediate timestep for the short-range non-bonded interactions, performing only bonded interactions every timestep.

- **Input and Output Compatibility.** The input and output file formats used by NAMD are identical to those used by CHARMM and X-PLOR. Input formats include coordinate files in PDB format[47], structure files in X-PLOR PSF format, and energy parameter files in either CHARMM or X-PLOR formats. Output formats include PDB coordinate files and binary DCD trajectory files. These similarities assure that the molecular dynamics trajectories from NAMD can be read by CHARMM or X-PLOR and that the user can exploit the many analysis algorithms of the latter packages.
- **Dynamics Simulation Options.** MD simulations may be carried out using several options, including
  - Constant energy dynamics,
  - Constant temperature dynamics via
    * Velocity rescaling,
    * Velocity reassignment,
    * Langevin dynamics,
  - Periodic boundary conditions,
  - Constant pressure dynamics via
    * Berendsen pressure coupling,
    * Nos-Hoover Langevin piston,
  - Energy minimization,
  - Fixed atoms,
  - Rigid waters,
  - Rigid bonds to hydrogen,
  - Harmonic restraints,

- Spherical or cylindrical boundary restraints.

- **Easy to Modify and Extend.** Another primary design objective for NAMD is extensibility and maintainability. In order to achieve this, it is designed in an object-oriented style with C++. Since molecular dynamics is a new field, new algorithms and techniques are continually being developed. NAMD's modular design allows one to integrate and test new algorithms easily. If you are contemplating a particular modification to NAMD you are encouraged to contact the developers at namd@ks.uiuc.edu for guidance.
- **Interactive MD simulations.** A system undergoing simulation in NAMD may be viewed and altered with VMD[48]; for instance, forces can be applied to a set of atoms to alter or rearrange part of the molecular structure.
- **Load Balancing.** An important factor in parallel applications is the equal distribution of computational load among the processors. In parallel molecular simulation, a spatial decomposition that evenly distributes the computational load causes the region of space mapped to each processor to become very irregular, hard to compute and difficult to generalize to the evaluation of many different types of forces. NAMD addresses this problem by using a simple uniform spatial decomposition where the entire model is split into uniform cubes of space called patches. An initial load balancer assigns patches and the calculation of interactions among the atoms within them to processors such that the computational load is balanced as much as possible. During the simulation, an incremental load balancer monitors the load and performs necessary adjustments.

## 2.3 Simulations

### 2.3.1 Study systems: The drop / The surface / The drop adsorbed on the surface

#### 2.3.1.1 The drop

At first a droplet of liquid had to be constructed at molecular dimensions. Water was chosen for convenience because i) it had already been subject to theoretical studies of physico-chemical properties of all various kinds, hence the level of acquainted knowledge on water must be considered high ii) it is well defined by several model descriptions, i.e. force fields, which is a crucial requirement for the intended type of study (molecular dynamics simulation). In addition, fluid phase behaviour had been shown to be well reproducible by the type of studies anticipated here[49].

A VMD[48] plug-in was used to construct a cubic box filled with water molecules. Subsequently a spherical volume was cut out from the water box using radii of different length. The two drops that had been taken into account in this study were of dimensions corresponding to 3,186 and 1,624 molecules respectively (figure 2.10).

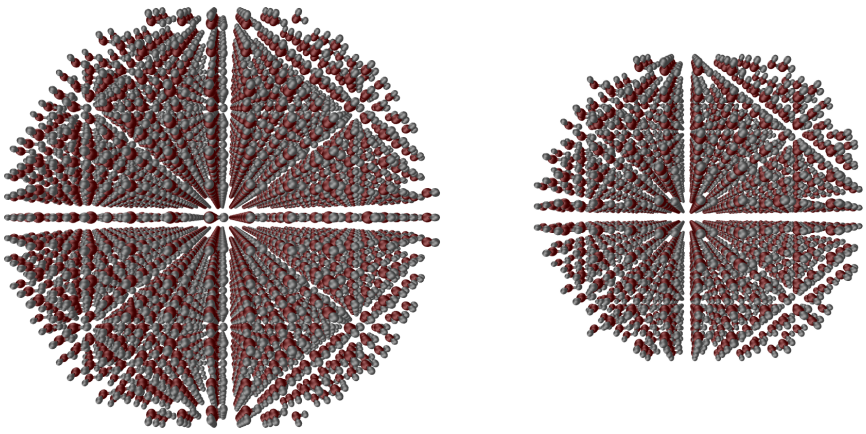

**Figure 2.10: The two spherical cutted drops.**

Short equilibration runs comprising 1.5 ps of Molecular Dynamics simulation (see section 2.2.2) at 300 $K$ are sufficient to maintain the spherical shape of the droplets.

This is assumed to result from the reproduction of surface tension effects (figure 2.11).

MD simulation conditions were:

- force field: SPC/E
- time step: 1.5 $fs$
- thermostat: Langevin coupling at 300 $K$
- cutoff: 11.0 Å
- environment: vacuum

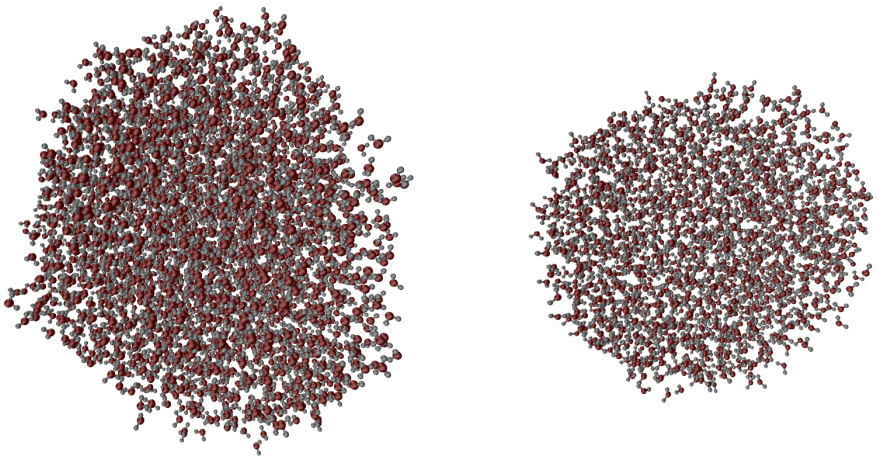

**Figure 2.11: Drops after 1.5 $ps$ of MD equilibration.**

#### 2.3.1.2 The surface

Next a reasonable method had to be developed to represent the molecular surface. At molecular-scale dimensions gravitation does not play a role. Liquid molecules are thus not deposited but rather simply adsorbed on the surface. The adsorption is facilitated by inter-molecular forces (of the non-bonded type, i.e. mediated by charges or van der Waals interactions). Such a situation can be realized either by explicit or implicit descriptions. In the simulations described here an implicit method had been preferred because of the associated gain in computational efficiency. The implicit surface is defined by a non-bonded potential similar to the Lennard-Jones potential,

$$V(r) = \frac{A}{r^{12}} - \frac{B}{r^6} \tag{2.35}$$

where $A$, $B$ are coefficients of repulsive and attractive van der Waals terms and $r$ denotes the center-center distance of a pair of atoms.

When a surface interacts simultaneously with many water molecules, all the couplings need to be considered by the implicit surface potential all at once. Hence instead of the usual decomposition into pairwise atom-atom interactions, with implicit surfaces there are one-to-many interactions to be taken into account. Theoretically, such a convolution of one-to-many interactions can be facilitated by a modification of the exponents in the distance terms of the Lennard Jones potential[1], thus the actually employed potential was of the type,

$$V(r) = \frac{A}{r^9} - \frac{B}{r^3} \tag{2.36}$$

In figure 2.12 these difference between the two types of Lennard Jones potential are graphically represented.

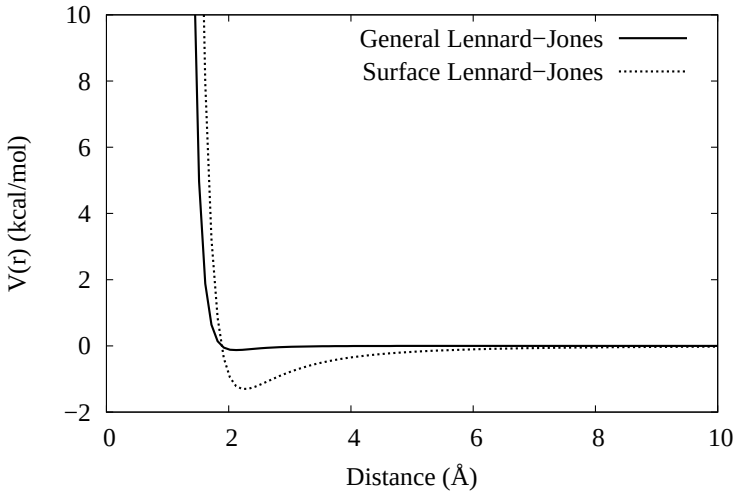


**Figure 2.12: Lennard-Jones and modified for surface potentials.**

#### 2.3.1.3 The drop adsorbed on the surface - different wettability

The coefficient, $B$, of the attractive term can be derived from the Hamaker constant of water on silicon dioxide, $1.1 \times 10^{-19}$ J, which leads us to a coefficient of 22.6 $kcal$ Å$^3$ $mol^{-1}$. The repulsive term may then be adjusted to reproduce the experimental contact angle of water droplets deposited on surfaces of identical composition[50].

In order to do so, $A$-values in between 400 and 2,000 $kcal$ Å$^9$ $mol^{-1}$ were examined including the implicit surface potential as a function of the $z$-coordinate:

$$V(z) = \frac{A}{z^9} - \frac{22.6}{z^3} \tag{2.37}$$

Initially droplets were positioned very close to the top layer of the surface, i.e. the z-coordinate of the lowest molecule was set to 2.0 Å. Then a 450 ps of MD equilibration was carried out to simulate the adsorption on the surface. Resulting contact angles are summarized in figure 2.13.

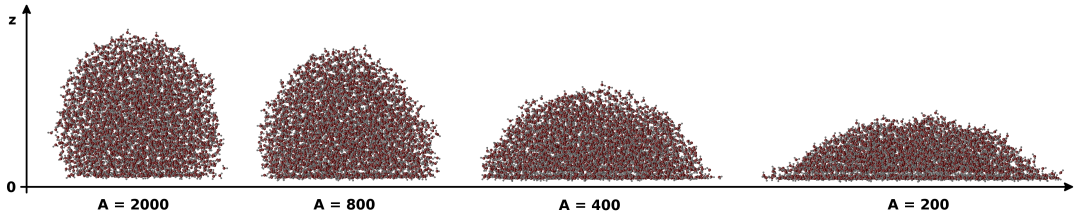


**Figure 2.13: Equilibration result for different repulsive terms.** $A$ in $kcal$ Å$^9$ $mol^{-1}$.

MD simulation conditions:

- force field: SPC/E
- time step: 1.5 $fs$
- thermostat: Langevin coupling at 300 $K$
- cut-off: 11.0 Å
- water molecules are rigid: no bond stretching and bending are considered
- the surface potential has a cut-off for distances $z \geq 25.0$ Å

### 2.3.2 Slippage simulations

#### 2.3.2.1 Surface with a gradient - step-like potentials

A theoretical model to reproduce the photo-induced surface gradient involves the following simple approximations:

- center the adsorbed droplet symmerically to $y = 0$ by shifting molecules about a constant translation vector
- impose the following case distinction:

$$\begin{aligned} & V(z) = \tfrac{A}{z^9} - \tfrac{22.6}{z^3} \\ where \quad & A = 1000 \qquad \forall\, y \leq 0.0 \text{ Å} \\ & A = 400 \qquad \forall\, y > 0.0 \text{ Å} \end{aligned} \tag{2.38}$$

In practice the above conditions will split droplet molecules into two groups where particles with $y > 0$ will be subject to an increased surface attraction ($A = 400$) as opposed to those having $y$-coordinates smaller than 0 ($A = 1000$). Indeed the drop appears to exhibit a lower contact angle on the right side ($y > 0$) when compared to the left side ($y < 0$).

Such an imbalance in surface attraction should result in a slippage in direction of the more attractive part of the surface (representation in figure 2.14).
A 3 $ns$ MD simulation was carried out to test the slippage hypothesis. The following conditions were applied:

- force field: SPC/E
- time step: 1.5 $fs$
- thermostat: Langevin coupling at 300 $K$
- cut-off: 11.0 Å
- water molecules are rigid: no bond stretching and bending are considered
- the surface potential is defined by Eq.2.38 up to a cut-off distance at $z \geq 25.0$ Å

Evidently, as graphically represented in figure 2.15, the drop did not move under such type of conditions.

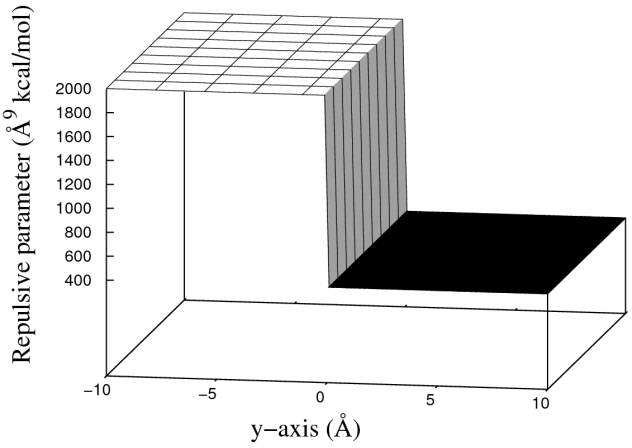


**Figure 2.14: Step-like potential representation.**

#### 2.3.2.2 Surface with a gradient - slide-like potentials

Due to the unsuccessful results obtained in the previous attempt regarding the representation of the photo-induced surface gradient, an improved definition of the surface potential was required.

One way to improve relationships was to introduce a smoother change of the potential around the $y = 0$ coordinate. For this purpose, the *Error Function*[51] was introduced, hence a continuous change of the repulsive term along the $y$-coordinate was implemented.

$$erf(x) = \sqrt{1 - exp(-x^2 \frac{\frac{4}{\pi} + ax^2}{1 + ax^2})} \quad with \quad a = \frac{8}{3\pi} \frac{\pi - 3}{4 - \pi} \tag{2.39}$$

The *Error Function* is used to define an $S(y)$ function that varies in the range $-1.0 < S(y) < 1.0$:

$$S(y) = \frac{1}{2}\, erf(\frac{y - \mu}{\sigma - \sqrt{2}}) + \frac{1}{2} \tag{2.40}$$

where $\mu$ is the central value with $S(y) = 1/2$ and $\sigma$ is the range of actual application

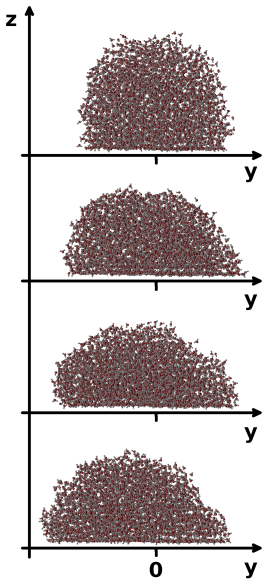


**Figure 2.15: Simulation snapshots of a surface adsorbed droplet under the influence of a step-like potential surface.** $y = 0$ and $z = 0$ are shown.

of the *Error Function*.

Introduction of $S(y)$ mainly affects the value of the repulsive term in the vicinity of $y = 0$, so the potential is now dependent on the $y$ coordinate in the following way,

$$V(y,z) = [1 - S(y)]\frac{A_1}{z^9} + S(y)\frac{A_2}{z^9} - \frac{22.6}{z^3} \tag{2.41}$$

Figure 2.16 shows the change of the repulsive term along the $y$-axis when using erf-related potentials.

A 3 $ns$ molecular dynamic simulation was carried out using the new slide-like potential. Conditions:

- force field: SPC/E
- time step: 1.5 $fs$
- Langevin thermal bath at 300 $K$
- cut-off: 11.0 Å
- water molecules are rigid: no bond stretching and bending are considered
- the surface potential is defined by Eq.2.41 and has a cut-off at $z \geq 25.0$ Å

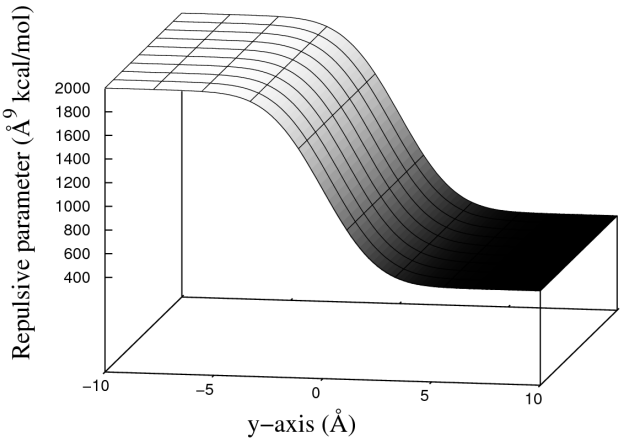


**Figure 2.16: Slide-like potential representation.**

- $\mu = 0$; $\sigma = 2.0$ Å; $A_1 = 1,000$ and $A_2 = 400$ $kcal$ Å$^9$ $mol^{-1}$

As shown in figure 2.17, using the new slide-like potential, the drop moves on until it is entirely on the more attractive side of the surface. During the slippage the advancing side contact angle is less than the one of the other side.

Also the smaller drop of 1,624 molecules of water on the same surface potential and in same condition slip on the surface, as shown in the figure 2.18.

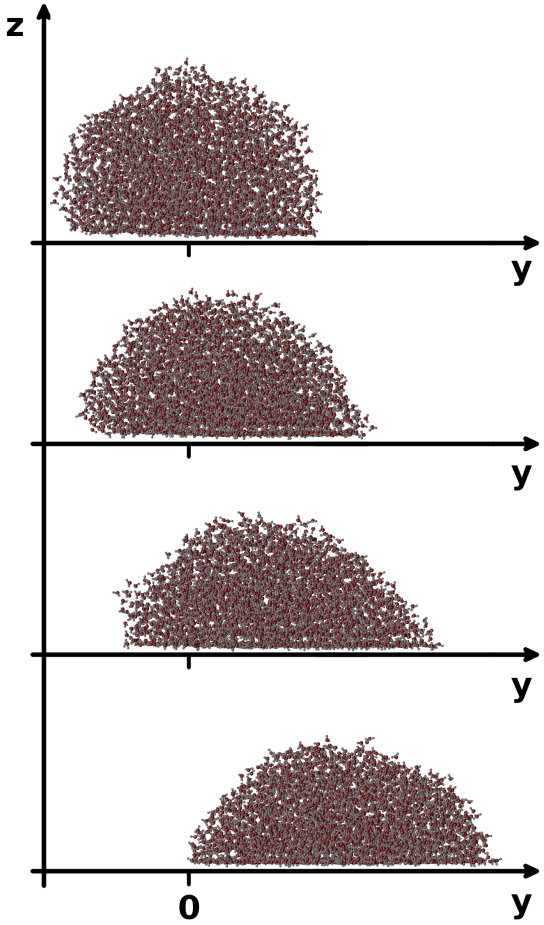


**Figure 2.17: 3** $ns$ **Simulation snapshots on step-like potential surface.** $y = 0$ and $z = 0$ are shown.

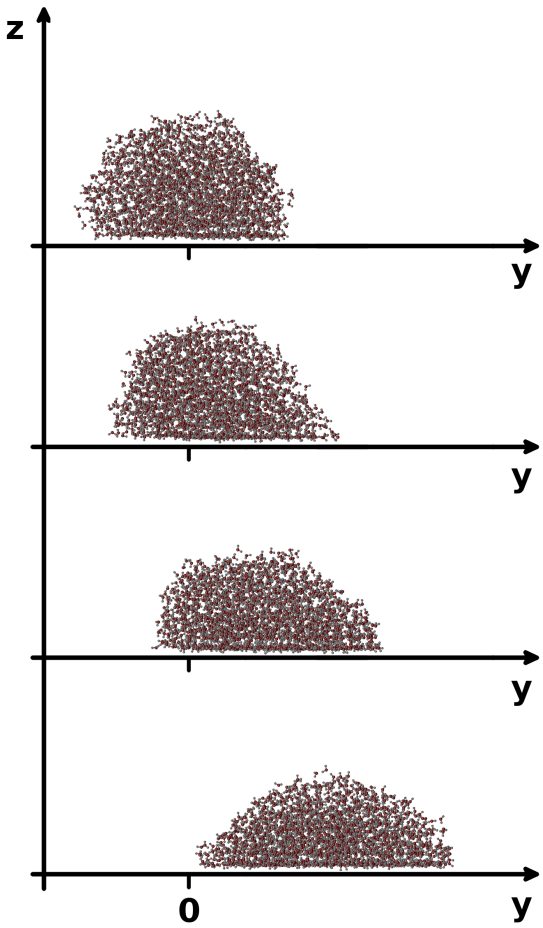


**Figure 2.18: 1.5 $ns$ Simulation snapshots on step-like potential surface of the smaller drop.** $y = 0$ and $z = 0$ are shown.

## 2.4 Analysis

### 2.4.1 Slippage velocity

In the following a summary shall be given listing the set of properties studied by means of MD simulation of the type discussed in the previous section 2.3.2.

The first observable taken into account was the center of mass (COM) movement of the droplet. Several parameters were changed to study the influence of individual components potentially affecting COM-movement.

The following parameters were examined:

- mass: simulation of different size droplets (1,624 or 3,186 molecules);
- $A_1 - A_2$: gap in the repulsive coefficients on either site of the surface potential;
- $\sigma$: variation of the application range of function $S(y)$;

#### 2.4.1.1 Different mass

The two droplet sizes taken into account gave rise to overall weights of $9.51 \times 10^{-20}$ $mg$ and $4.85 \times 10^{-20}$ $mg$ respectively.
MD simulations were carried out using the parameters and setup described in section 2.3.2.2. Figure 2.19 summarizes COM-movement with particular emphasis on the $y$-coordinate, i.e. the axis parallel to the surface on which droplet movement occurs.
Since the driving force of droplet slippage is expected to be constant in the two systems studied, it is reasonable to observe the smaller droplet moving faster than the larger one. Approximative COM velocities were $\sim 36$ Å$/ns$ and $\sim 26$ Å$/ns$ respectively.

The same type of analysis was carried out, again comparing the two droplet sizes, but now increasing the gap in repulsive parameters to values of $A_1 = 2,000$ and $A_2 = 400$ $kcal$ Å$^9$ $mol^{-1}$; Results are plotted in figure 2.20 which confirm the previous finding that smaller drops translocate faster: derived velocities were on the order of $\sim 60$ Å$/ns$ and $\sim 34$ Å$/ns$.

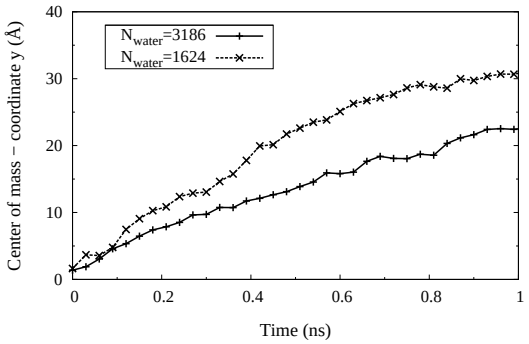


**Figure 2.19: $y$-coordinate of the center of mass of differently sized droplets and evolution over MD simulation time.** $A_1 = 1000$; $A_2 = 400$; $\sigma = 2.0$.

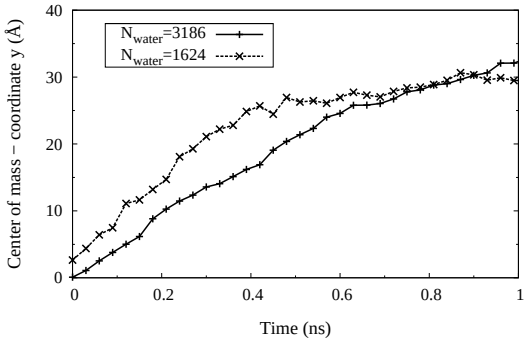


**Figure 2.20: $y$-coordinate of the center of mass of differently sized droplets at increased $A_{1/2}$ gap and evolution over MD simulation time.** $A_1 = 2000$; $A_2 = 400$; $\sigma = 2.0$

#### 2.4.1.2 Gap in repulsive coefficients $A_{1/2}$

The center of mass movement was re-analysed for a series of increasing gaps in repulsive coefficients $A_{1/2}$ providing the driving force of slippage. $A_2$ was kept constant while $A_1$ was steadily increased. Results are summarized in figure 2.21 where an example of the step-like potential is also included for comparison.
From figure 2.21 it becomes clear that COM velocity is a function of the gap in re-

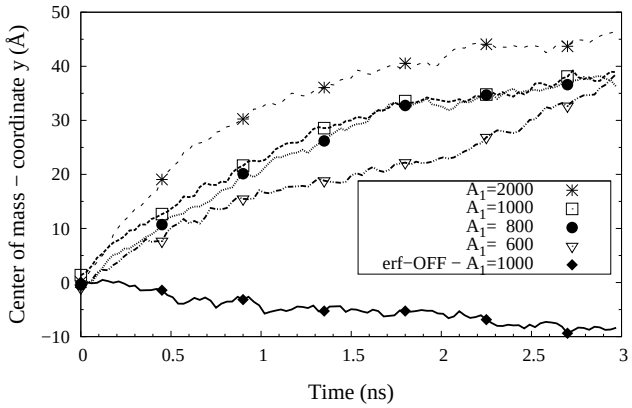


**Figure 2.21: $y$-coordinate of COMs of large droplets comprising 3,186 water molecules for a series of increasing $A_{1/2}$ gaps and evolution over MD simulation time.** $A_2 = 400\ kcal\ Å^9\ mol^{-1}$; $\sigma = 2.0$ Å.

pulsive coefficients $A_{1/2}$ and increasing the latter will accelerate the process of droplet translocation. A detailed listing of determined translocation velocities is given in table 2.1.

| $\mathbf{A_1}$ | $\mathbf{A_2}$ | **v** |
|---|---|---|
| $(kcal$ Å$^9$ $mol^{-1}$ $)$ | | $(Å/ns)$ |
| 2000 | 400 | $\sim 34$ |
| 1000 | 400 | $\sim 26$ |
| 800 | 400 | $\sim 20$ |
| 600 | 400 | $\sim 15$ |

**Table 2.1:** Velocities determined for various gaps in repulsive coefficients $A_{1/2}$.

#### 2.4.1.3 Slide width $\sigma$

It is interesting to investigate the influence of parameter $\sigma$ (see eq. 2.39) for cases where slipping occurs, i.e. at moderate gap sizes regarding repulsive coefficients $A_{1/2}$. A corresponding analysis is presented in figures 2.22 and 2.23 which appear to point to a somewhat optimal setting at $\sigma = 2.0$ Å.

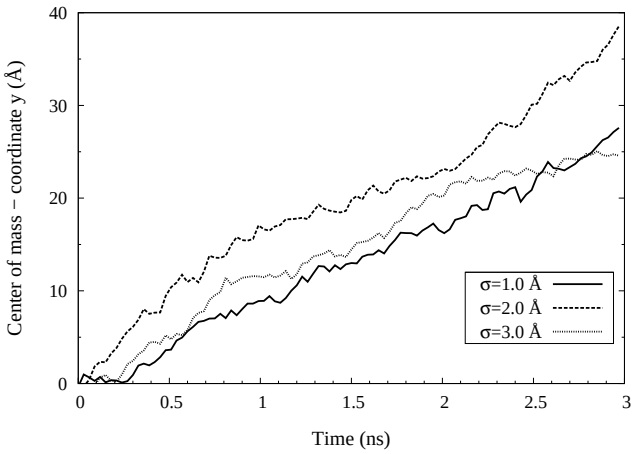


**Figure 2.22: $y$ coordinate of COM of a large droplet comprising 3,186 water molecules at varying slide width $\sigma$.** $A_1 = 600$; $A_2 = 400$ $kcal$ Å$^9$ $mol^{-1}$

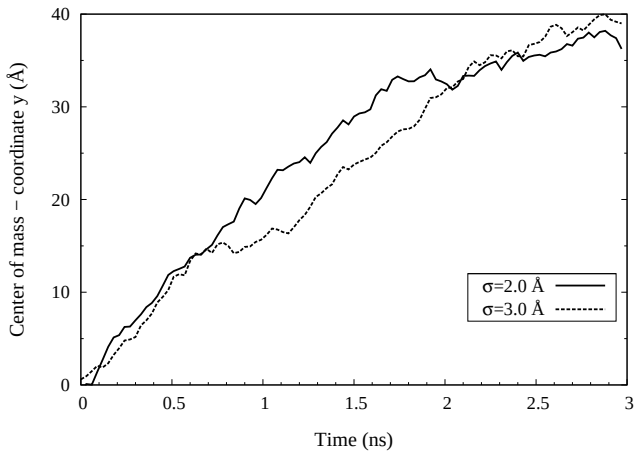


**Figure 2.23:** $y$ **coordinate of COM of a large droplet comprising 3,186 water molecules at varying slide width** $\sigma$**.** $A_1 = 800$; $A_2 = 400\ kcal\ \text{Å}^9\ mol^{-1}$

### 2.4.2 Efforts to identify elements constituting the driving force of droplet slippage

As mentioned previously the droplet experiences different slippage tendencies when applying a step-like or a slide-like potential. Only in the latter case the droplet can actually be set into motion. In an effort to get a somewhat better understanding of what molecular factors do provide the driving force to the translocation process, several additional studies have been carried out thereby carefully looking into the domain of potential change (i.e. around $y = 0$).

A set of different properties was computed in local subcompartments (see the $xyz$-boxes indicated in black in figure 2.24) and compared to each other. Such a spatial

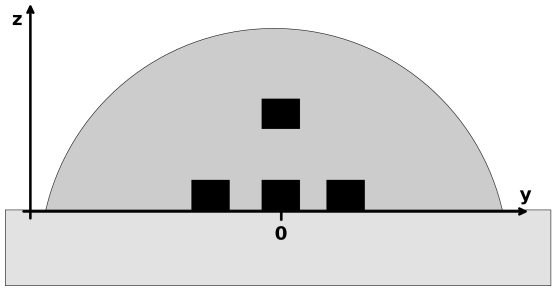


**Figure 2.24: Graphical representation of local boxes (black squares) to which property calculation is restricted.**

comparison could under ideal circumstances reveal important insights into molecular mechanisms affecting droplet movement. Here a comparison of properties derived under application of a step-like potential (unable to induce slippage) with properties determined under application of the slide-like potential (capable of slippage induction) could help to identify that set of molecular properties that is responsible for the overall process. Apparently this would be a property that turns out to be very different in the case of a step-like potential when compared to a situation where a slide-like potential is applied. The following list of properties was taken into account:

- Local density: determined via the average number of molecules found inside small local boxes,

- Residence time: i.e. the average time that water molecules remain inside small local boxes,
- H-bonds: average number of hydrogen bonds formed inside small local boxes,
- Water dipoles: dipole orientation and dipole-dipole interactions always taking into account only that subset of water molecules confined to a particular local box,
- Diffusion coefficients: how fast water molecules diffuse inside small local subcompartments,

#### 2.4.2.1 Density

The droplet domain on the surface was decomposed into small boxes of dimensions $10 \times 3 \times 4$ Å for $x, y, z$ dimensions, respectively. Main emphasis was on the area around the $y = 0$ and $z = 0$. Individual densities were computed and averaged over consecutive windows always sampling 150 $ps$ of MD simulation. This way different phases of the slippage process may be distinguished, for example an initial starting interval (15–150 $ps$), an intermediary movement phase (300–450 $ps$) and a final deceleration phase (600–750 $ps$).

For comparison — and potential identification of significant differences — an identical calculation was also carried out under application of a step-like potential.

Results are depicted in figures 2.25, 2.26, 2.27 but no obvious difference can be identified between individual runs (compare solid to dashed curves in figures). Partial densities accumulate gradually around $y = 0$ because of the more attractive potential starting to be "felt" about that location. Lack of density for the $y < 0$ domain in figure 2.27 is due to the late stage of droplet translocation where most of the droplet is already adsorbed on the more attractive side of the surface.

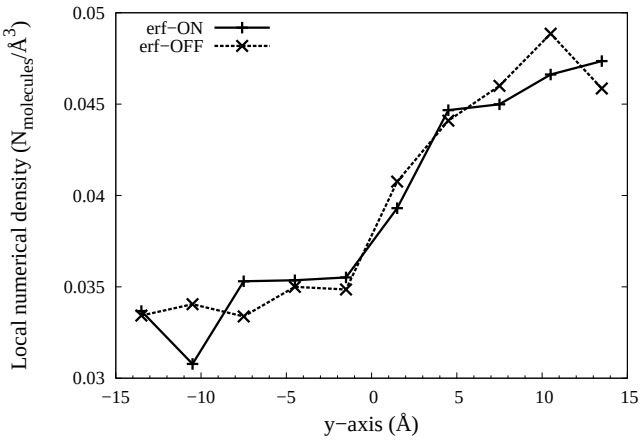


**Figure 2.25: Partial density analysis along the $y$-axis - 15–150 $ps$.** initial phase; the drop is accelerating

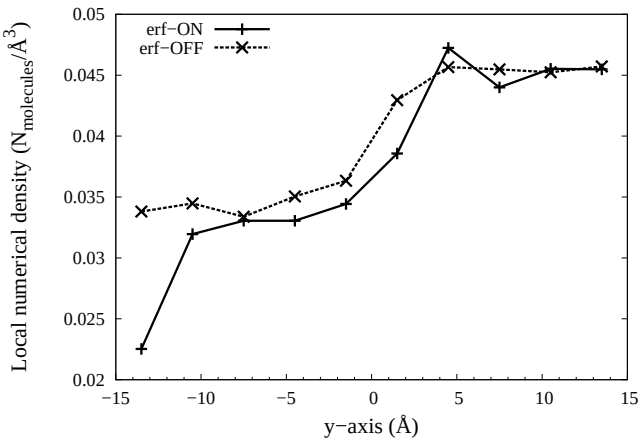


**Figure 2.26: Partial density analysis along the $y$-axis - 300–450 $ps$.** intermediary phase; the drop is "slipping" in direction $y > 0$

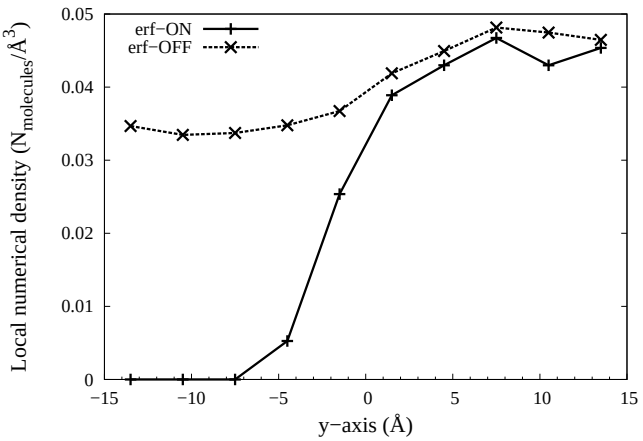


**Figure 2.27: Partial density analysis along the $y$-axis - 600–750 $ps$.** final phase; the drop is almost entirely on the side of the more attractive potential

#### 2.4.2.2 Residence time

Differences between a step-like and a slide-like potential were tried to be identified via residence time analysis. Focus was again on the region adjacent to the potential gap. The method used to analyze residence times was similar to the one reported in the literature[52, 53].

Results are shown in figure 2.28 always sampling time windows of 50 $ps$ in a local box defined by $-2.0 < y < 2.0$ and $z < 5.0$. Horizontal lines indicate reference behaviour on hydrophobic surface ($A = 2000$, dashed line) and hydrophilic surface ($A = 400$, solid line) of the surface.

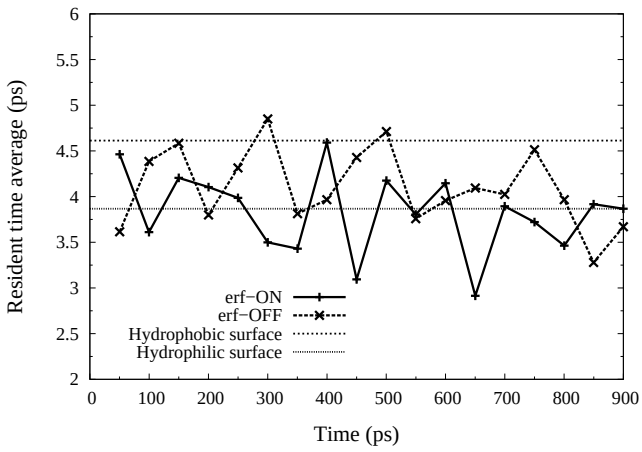


**Figure 2.28: Residence times.** Calculated in a selected local box close to the switching point of severe potential change showing averages over 50 $ps$ windows always

Residence times ($R_t$) were then computed in different zones of the droplet for different instances in the MD simulation. Some indicative results are summarized in table 2.2: despite the significant degree of scatter, several important observations could be made:

- $R_t$ on the "hydrophilic" side ($3 < y < 5$) is smaller than the reference (compare to value for $A = 400$) while for the "hydrophobic" side ($-5 < y < -3$) $R_t$ is rather similar to the reference (compare to value for $A = 2000$). These data suggest that the spread of molecules is faster on the hydrophilic side irrespective of the type of potential applied.

- When the drop starts moving (15–150 $ps$) molecules are slower on the "slide"-like descent than they are on a "step"-like descent. Later on $R_t$s become very similar to each other.

| | 15–150 $ps$ | | 300-450 $ps$ | | 600–750 $ps$ | |
|---|---|---|---|---|---|---|
| $z < 3$ | erf-ON | erf-OFF | erf-ON | erf-OFF | erf-ON | erf-OFF |
| $-1 < y < 1$ | 4.48 | 3.15 | 4.00 | 4.03 | 3.35 | 3.72 |
| $-5 < y < -3$ | 3.92 | 3.92 | 3.80 | 3.84 | 2.40 | 3.81 |
| $3 < y < 5$ | 3.33 | 3.84 | 4.11 | 3.84 | 3.96 | 4.24 |
| $A = 2000$ | 3.87 | | | | | |
| $A = 400$ | 4.61 | | | | | |

**Table 2.2:** Residence times in several zones at different instances of MD simulation ($ps$)

Referring to the drop-on-a-surface simulation without changes in the surface potential (i.e. neither step- nor slide-like types), there is a notable difference in local residence times for simulations with applied surface potentials of changing character regardless of the actual outcome of the simulation. In other words, even for a step-like potential, already found to be incapable of triggering actual droplet translocation, as far as residence times are concerned there is a difference noticeable when comparing to the static case of a droplet adsorbed on a surface (verified by the application of a homogeneous potential). However, no significant differences in residence times were detected between slide-like and step-like potentials.

#### 2.4.2.3 Hydrogen bonds

The average number of hydrogen bonds ($N_H$) was computed in small boxes distributed throughout the droplet domain. Standard H-bond assignment was employed following previous reports[54, 55]. In particular, the oxygen-oxygen distance was required to be less than 3.5 Å and the O–H $\cdots$ O angle to be less than 30° for a H-bond to be assigned.

Table 2.3 summarizes a subset of the results obtained:

- The number of established H-bonds is reduced on the "slide"-like potential when compared to the "step"-like potential (or also the case of increased potential gap). This suggests that on the "slide"-like potential water molecules face considerable difficulties in maintaining H-bonds, which also implies that molecular motions there seem to occur in largely increased disorder.
- A smaller number of H-bonds is formed on the "hydrophilic" side of the surface.

| | 15–150 *ps* | | 300-450 *ps* | | 600–750 *ps* | |
|---|---|---|---|---|---|---|
| $z < 3$ | erf-ON | erf-OFF | erf-ON | erf-OFF | erf-ON | erf-OFF |
| $-1 < y < 1$ | 5.30 | 5.41 | 6.19 | 7.45 | 3.65 | 8.27 |
| $-5 < y < -3$ | 4.46 | 4.65 | 4.25 | 5.33 | 0.34 | 6.13 |
| $3 < y < 5$ | 3.33 | 3.84 | 4.11 | 3.84 | 3.96 | 4.24 |
| $A = 2000$ | 12.85 | | | | | |
| $A = 400$ | 5.38 | | | | | |

**Table 2.3:** Average numbers of hydrogen-bonds formed in different zones at different instances of MD simulation.

Analogous to the effect observed for residence times, inclusion of any type of surface potentials of varying character will lead to a change in hydrogen-bond formation when compared to the static case of a homogeneous surface. Contrary to residence times for H-bonds, however, slight differences are revealed between "slide"- and "step"-like potentials.

#### 2.4.2.4 Diffusion coefficient

The next property to study on a local level was diffusion. Coefficients were computed according to the Einstein-Smoluchowski relation[56, 57, 58, 59, 60] applying the squared-path $< r^2 >$ variant.

On the "slide"-like descent molecules show increased diffusion coefficients when compared to the "step"-like descent. Consequently, molecules appear to become accelerated in the domain where the repulsive parameter $A$ changes abruptly, which may ease the movement over to the "hydrophilic" part of the surface.

| $z < 3$ | erf-ON | erf-OFF |
|---|---|---|
| $-1 < y < 1$ | 5.05 | 2.85 |
| $-5 < y < -3$ | 4.14 | 3.33 |
| $3 < y < 5$ | 4.65 | 3.15 |
| $A = 2000$ | 2.44 | |
| $A = 400$ | 3.44 | |

**Table 2.4:** Mean diffusion coefficients averaged over 150 $ps$ ($\times 10^{-9}$ $m^2/s$)

#### 2.4.2.5 Dipole orientation and dipole-dipole interaction energies

A final property investigated was the distribution of dipoles and the related dipole-mediated phenomena. At first the average dipole orientation along the slippage direction ($y$-axis) was taken into account. This was motivated by the intention to detect potential changes occurring during the slippage phase. The following protocol was applied:

- for all dipoles falling into a small box element compute the y-component of the dipole; this is done from a simple cosine relation regarding the angle between the dipole axis and the y-axis, hence symmetry is established with respect to an angle of 90°;
- form the average over all individual y-components;
- form one more average over all snapshots falling into a particular time window of MD simulation;

Resulting average y-components of dipoles are shown in table 2.5. Here $d_{or} = 0$ means all dipoles are perpendicular to the y-axis whereas $d_{or} = 1$ would imply all the dipoles are parallel to the $y$-axis. From table 2.5 we get the impression that until 150 $ps$ dipoles are marginally more parallel to the surface on the "slide"-like descent than they are on the "step"-like descent. For later stages (300-450 $ps$, 600-750 $ps$) the opposite may be said, i.e. dipoles are a little more perpendicular to the surface when using the "slide"-like potential as compared to the "step"-like potential.

Next dipole-dipole interaction energies were computed and results are summarized in table 2.6.

| | 15–150 $ps$ | | 300-450 $ps$ | | 600–750 $ps$ | |
|---|---|---|---|---|---|---|
| $z < 3$ | erf-ON | erf-OFF | erf-ON | erf-OFF | erf-ON | erf-OFF |
| $-1 < y < 1$ | 0.559 | 0.537 | 0.547 | 0.558 | 0.512 | 0.551 |
| $-5 < y < -3$ | 0.577 | 0.542 | 0.545 | 0.576 | 0.347 | 0.572 |
| $3 < y < 5$ | 0.546 | 0.561 | 0.533 | 0.561 | 0.533 | 0.549 |
| $A = 2000$ | 0.569 | | | | | |
| $A = 400$ | 0.543 | | | | | |

**Table 2.5:** Mean water dipole orientations in selected zones at different stages of droplet translocation

On the "step"-like descent dipole-dipole interaction energies turned out to be stronger than on the "slide"-like descent, thus water molecules seem to be stabilized on the "step"-like making it "harder" for them to move over to the hydrophilic side. However, making it over to the hydrophilic side somehow results in deepening of interaction strength (dipole-dipole potential energies become deeper, i.e. more stable).

| | 15–150 $ps$ | | 300-450 $ps$ | | 600–750 $ps$ | |
|---|---|---|---|---|---|---|
| $z < 3$ | erf-ON | erf-OFF | erf-ON | erf-OFF | erf-ON | erf-OFF |
| $-1 < y < 1$ | -0.253 | -0.289 | -0.255 | -0.285 | -0.226 | -0.263 |
| $-5 < y < -3$ | -0.196 | -0.230 | -0.206 | -0.201 | -0.262 | -0.209 |
| $3 < y < 5$ | -0.386 | -0.354 | -0.363 | -0.386 | -0.374 | -0.351 |
| $A = 2000$ | -0.203 | | | | | |
| $A = 400$ | -0.379 | | | | | |

**Table 2.6:** Average dipole-dipole interaction energies in selected zones at different stages of droplet slippage ($kcal\ mol^{-1}\ molecule^{-1}$)

## 2.5 Final considerations about droplet slippage investigation

Summarizing this first part concerned with a slipping drop on a functionalized surface, it is remarkable to observe that on the "slide"-like potential switch water molecules appear to be moving much faster than on the "step"-like one.

Dipole cross-correlation with respect to the direction of droplet translocation appears markedly increased (parallel as well as anti-parallel orientations) especially for the initial period when the droplet starts to move.

In addition, the strength of dipole-dipole interaction is decreased in the vicinity of the "slide" profile as opposed to the "step" one also pointing to an increased number of dipole pairs in parallel orientation.

A likely scenario for the microscopic mode of action of droplet slippage was that the "slide"-like surface potential causes an increase in the less energetic parallel alignment of dipoles directed towards the "hydrophilic" part of the surface, thus pushing the suboptimally aligned dipoles forward to "liberate" them. The dipoles seek new conformations in the more stable anti-parallel alignments thereby pushing forward the core of the drop and eventually the entire drop.

# 3

# Mesoscopic study of snowflake fractals melting

## 3.1 von Koch fractal

Since its formalization fractals represent a fundamental tool to solve theoretical and applied problems which in nature cannot be identified by analytical curves. The self similarity property, i.e. the fact that the figure looks always the same independently of the magnitude order, allowed to apply this concept in problems where scaling comes out.

Helge von Koch introduced the so called von Koch island at the beginnings of the twentieth century[7].
The Koch curve can be constructed by starting with an equilateral triangle, then recursively altering each line segment as follows:

- divide the line segment into three segments of equal length.
- draw an equilateral triangle that has the middle segment from step 1 as its base and points outward.
- remove the line segment that is the base of the triangle from step 2.

After one iteration of this process, the result is a shape similar to the Star of David. The Koch curve is the limit approached as the above steps are followed over and over again.

The Koch curve has an infinite length because each time the steps above are performed on each line segment of the figure there are four times as many line segments,

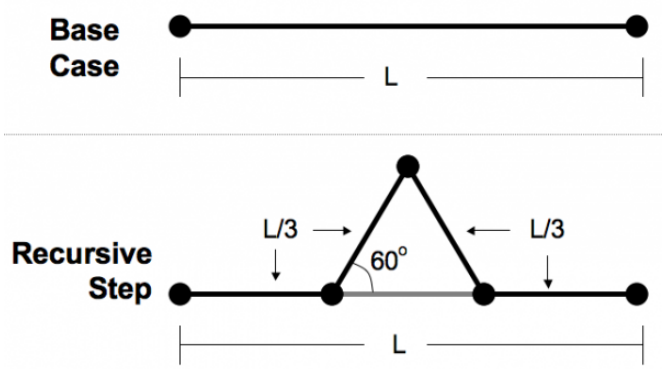


**Figure 3.1: von Koch curve construction step.**

the length of each being one-third the length of the segments in the previous stage. Hence the total length increases by one third and thus the length at step $n$ will be $\frac{4}{3}n$ of the original triangle perimeter: the fractal dimension[61] is $\frac{\log 4}{\log 3} \approx 1.262$, greater than the euclidean dimension of a line (1) but less than the plane one (2).

Besides its beauty, the von Koch curve is often used to test fractal algorithms because its fractal dimension is known, and it found applications in different fields of science[62]. Moreover because of its hexagonal symmetry, a filled von Koch island is a good candidate (see figure 3.2) to represent a snowflake[63].

## 3.2 Development of a new simulation algorithm

The fundamental computational methods, on which the developed new algorithm is based, are kinetic Monte Carlo[64] and Random Walk[65].

The kinetic Monte Carlo is a Monte Carlo method computer simulation intended to simulate the time evolution of some processes occurring in nature. Typically these are processes that occur with a given known rate.
It works generating random new configurations at each time step. Following suitable specific criteria the new configurations can be accepted or not.

Random Walk is a random process consisting of a sequence of discrete steps of fixed length. The random thermal perturbations in a liquid are responsible for random walk phenomenons like the Brownian motion. The collisions of molecules in the gas phase

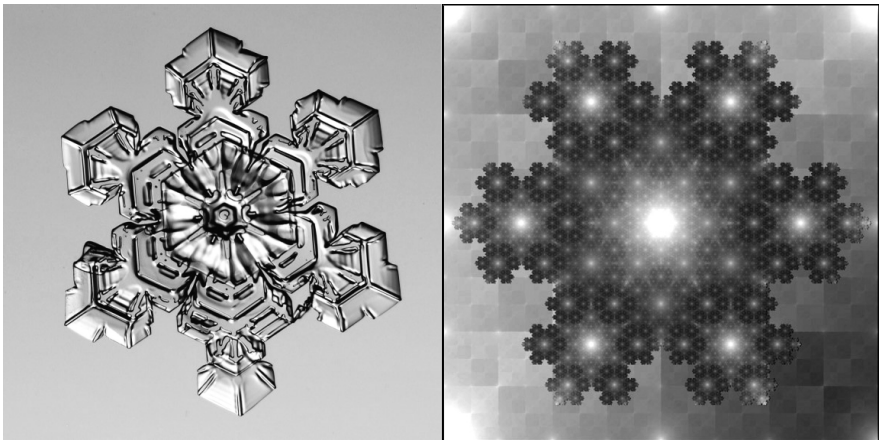

**Figure 3.2: Snowflake photo and von Koch fractal representation.**

are random walks that yield to specific diffusion[58, 59].
The study of random walks on lattices along the last decades had a huge development aimed by their many potential applications. While the basic works started from simple lattices with integer Euclidean dimension[66, 67, 68], in recent years the attention has focused on more and more complex underlying geometries.

### 3.2.1 Snow-fractal building

The snow crystal was built by means of a coarse grain approximation, which consists of a bi-dimensional set of beads, spread in hexagonal fashion according to the symmetries of the von Koch fractal. The procedure to construct a filled von Koch-like aggregate, displayed in figure 3.3, is resumed in two stages. First the position of the peripheral beads is determined and then all beads which correspond to the lattice nodes inside the fractal are added:

- the construction starts assigning to one single beads the coordinates $(1, 0)$; the following four maps are applied to this point:

$$\begin{cases} x_{n+1} = & \frac{1}{3}x_n \\ y_{n+1} = & \frac{1}{3}y_n \end{cases}, \tag{3.1}$$

$$\begin{cases} x_{n+1} = & \frac{1}{3}\cos\left(\frac{\pi}{3}\right)x_n - \frac{1}{3}\sin\left(\frac{\pi}{3}\right)y_n + \frac{1}{3} \\ y_{n+1} = & \frac{1}{3}\sin\left(\frac{\pi}{3}\right)x_n + \frac{1}{3}\cos\left(\frac{\pi}{3}\right)y_n \end{cases}, \tag{3.2}$$

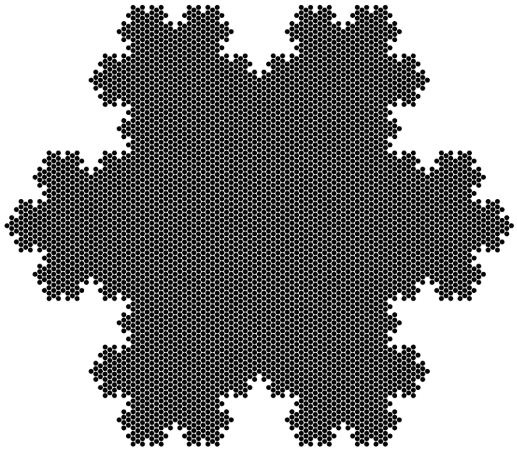

**Figure 3.3: Builded filled $4^{th}$ generation von Koch snow crystal.**

$$\begin{cases} x_{n+1} = & \frac{1}{3}\cos(\frac{2\pi}{3})x_n - \frac{1}{3}\sin(\frac{2\pi}{3})y_n + \frac{1}{2} \\ y_{n+1} = & \frac{1}{3}\sin(\frac{2\pi}{3})x_n + \frac{1}{3}\cos(\frac{2\pi}{3})y_n + \frac{\sqrt{3}}{2} \end{cases} \quad \text{and} \tag{3.3}$$

$$\begin{cases} x_{n+1} = & \frac{1}{3}x_n + \frac{2}{3} \\ y_{n+1} = & \frac{1}{3}y_n \end{cases} . \tag{3.4}$$

In this way four new beads are obtained to which the same four maps will applied again.

- This procedure is repeated $g$ times, with $g$ the required fractal generation. At this stage just one third of the perimeter, consisting of $4^g$ points, is built.
- To complete the perimeter, to every point of the set we apply:

  1) symmetry with respect to the axis $y = 0$ and clockwise rotation of $60^o$ around the point (0,0).

  2) symmetry with respect to the axis $y = 0$ and counter clockwise rotation of $60^o$ around the point (1,0).

Thus the peripheral beads of the structure are determined with the above procedure. The minimal distance between the beads results in $\epsilon_g = 1/3^g$.

The region inside the perimeter line has to be completely filled by nodes which have a minimal distance equal to $\epsilon_g$ in hexagonal fashion. A specific algorithm was

developed which works as an involving spiral covering all the inside space until ending in the central node of the snow crystal.
The peripheral walkers are $N_p = 3 \cdot 4^{g-1}$ and the total number of walkers is given by $N = 1 + 3\sum_{j=1}^{g} 4^{g-j+\delta_{jg}} \sum_{m=1}^{3^{j-1}} m$.

The amount of the peripheral (solid line) and of all beads (dashed line) is compared in figure 3.4; they are plotted versus the reciprocal of the minimal distance between the nodes of the lattice in double logarithmic scale to basis 10.

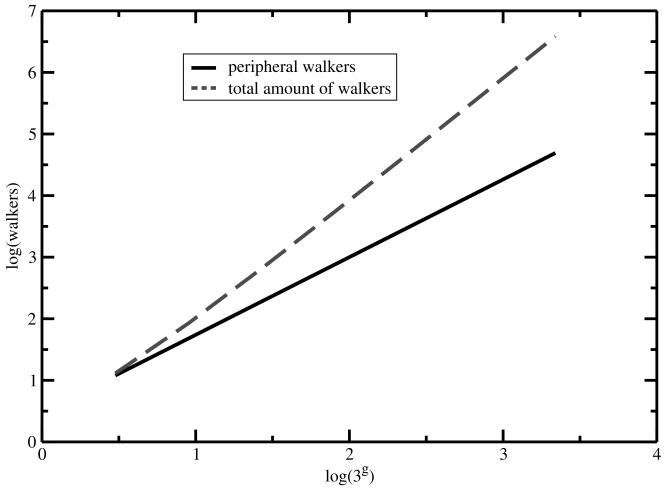


**Figure 3.4: Peripheral and total amount of beads.** Number of beads versus the reciprocal of the minimal distance between them in double logarithmic scale to basis 10. The dashed line represents the total amount of beads, while the solid line *only* the peripheral ones.

The solid line shows a straight line with slope $m = d_f$ as it should be. The dashed line corresponding to the total number of walkers, shows a non linear behavior. Indeed for low values on $x$-axis, i.e. at low generations, the peripheral walkers are predominant and they tend to reduce the slope. For big values of $g$ the peripheral nodes become a negligible portion and the structure can be approximated to a two dimensional structure; thus asymptotically $m \to 2$, corresponding to the euclidean dimension of a plain.

### 3.2.2 Lattice definition

In order to produce Random Walk of the previous defined beads, it is necessary to define a bi-dimensional lattice of positions where the "walkers" could move. The symmetry of the filled von Koch fractal is hexagonal. Therefore the lattice is composed of points which are defined by the vertex of packed hexagons (i.e. like a honey comb) including their centers (figure 3.5). So all the bead positions can lay on the lattice. The symmetry of such a lattice is triangular.

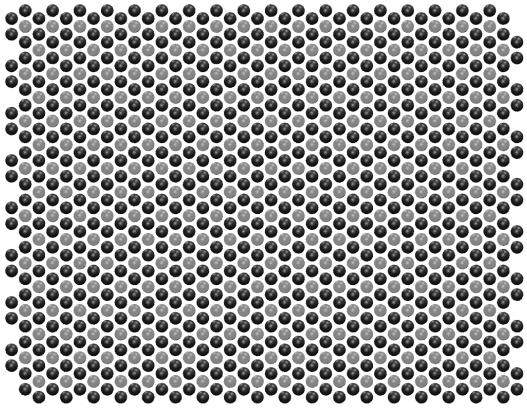

**Figure 3.5: Lattice representation.** hexagons in dark, them centers in bright.

The minimal internodal distance is set equal to the crystal's interbead distance in such a way that every vertex of the fractal matches with a node of the lattice. The lattice size is defined as big as the boundary conditions substantially do not influence the crystal dynamics.

Then the central bead of the built snow-fractal is associated with the central node of this lattice (figure 3.6). In this way the whole structure lays on the lattice and one can get rid of the Cartesian coordinates by using the labels assigned to the lattice's nodes. This trick gives the possibility to study very big structures because of dealing with $N$ (number of beads) integer labels instead of $2N$ double precision coordinates.

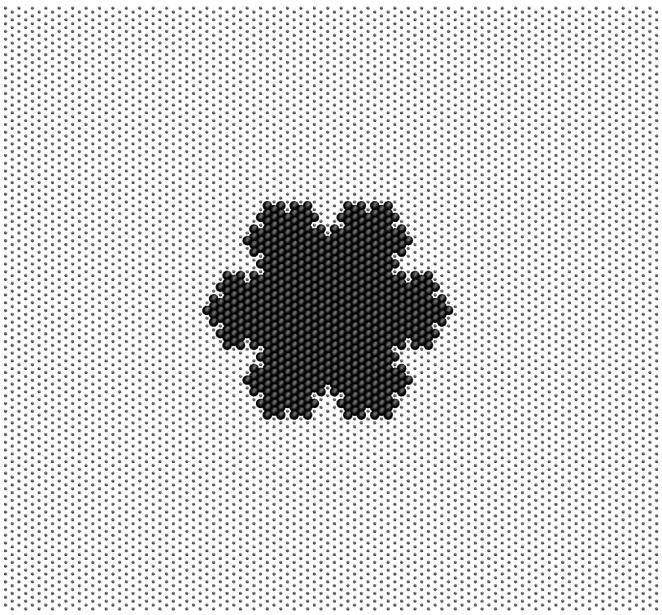

**Figure 3.6: Lattice representation.** beads in black, lattice points in gray.

### 3.2.3 Simulation algorithm - $MCRWS$

As described before, the simulation is based on random walks of the beads on an equilateral triangular lattice. The set conditions are:

- the nodes of the snowflake are the initial position of the walkers
- the walkers motion is random
- every walker can move from its site to a free nearest neighbor (walkers overlapping is not allowed)

In order to consider the interaction between two beads, a short range attractive potential parameter ($U$) was defined. Via this parameter the probability that a walker can move is calculated according to the equation:

$$P(n, i, U, T) = \frac{i \exp\left(-iU/k_B T\right)}{n - i + i \exp\left(-iU/k_B T\right)} \tag{3.5}$$

where $n$ is the number of the nearest lattice sites, which equals 6 for the internal nodes

and assumes value 3 or 5 on the boundaries. The variable $i$ indicates the number of occupied nearest sites ($i = 1, \ldots, 6$), so that the probability to move decreases significantly if the walker is in contact with other walkers. $T$ is the temperature in Kelvin and $k_B$ the Boltzmann constant.

The developed algorithm to simulate the time evolution of the system is based on the following steps:

- at each time step a bead is randomly chosen; the bead has to be free to move, i.e. have free lattice nodes around
- its probability to move is calculated and evaluated as condition to accept a new configuration (as done in Monte Carlo methods).
- the beads moves to one of the free "neighbor" node with the probability $[1 - P(n, i, U, T)]/(n - i)$
- these steps are repeated cyclically for every time step

Further conditions are:

- once a bead is detached from the snow-fractal core the initially taken direction is maintained as preferential until it "encounter" another bead. A slight probability to deviate if perturbation occurs is considered. This condition is fully justified by the fact that the walker conserves its momentum, being a simulation at mesoscopic scale.
- once a bead reaches a lattice boundary its motion stops definitely because it is considered far enough from the core.

In figure 3.7 some snapshots are reported for the time evolution simulation of a $5^{th}$ generation von Koch-like fractal.

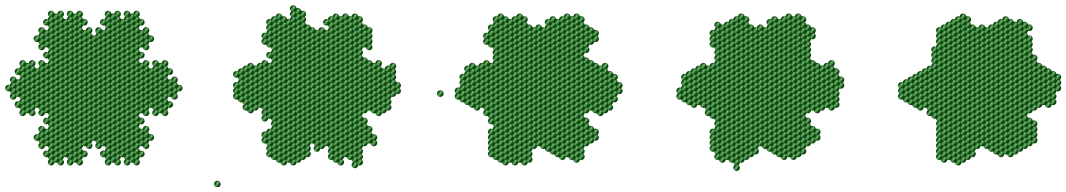

**Figure 3.7: Simulation snapshots of a von Koch crystal of generation $3^{rd}$.**

The defined attractive potential between the beads maintain the fractal core during simulation. The tips on the border are the first beads that leave the core, in accordance with their lower number of attraction interactions with other beads.

## 3.3 Ice parameter derivation

In order to validate the new simulation method and to parameterize the $U$ value that reproduce snowflakes ice crystal water interactions, $MCRWS$ was compared with Molecular Dynamics simulations ($MDS$). An ice crystal constituted by 9 layers was cut to get a $3^{rd}$ generation filled von Koch-like structure (in figure 3.8).

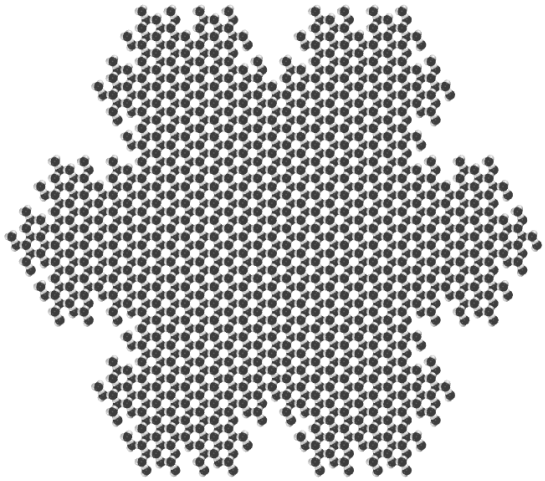

**Figure 3.8: Ice crystal generated for Molecular Dynamics simulation.**

The initial structure was built by placing a cell unit of the ice structure of $2 \times 9$ water molecules in coordinates that corresponds to the $3^{rd}$ generation walkers positions. This is reasonable for the hexagonal structure of the ice. A perfect ice crystal structure was reproduced replicating the cell in the six directions with a distance of 4.514 Å.

The MDS were carried out with the AMBER [69] suite of programs.
Water molecules were described by TIP4P/Ice [70], a specifically developed water model for liquid/solid equilibria close to the freezing point of water.
In the TIP4P water model, water molecule is represented by 4 sites: oxygen, two hydrogens and a dummy atom placed near the oxygen along the bisector of the HOH angle (see figure 3.9).

If the molecules are considered rigid, the potential is defined just by the intermolecular forces.

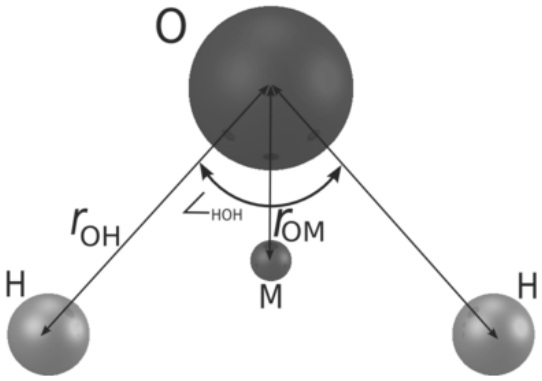


**Figure 3.9: TIP4P/Ice water model sites.**

The electrostatic interaction is modeled using Coulomb's law: the positive charges are placed on the hydogens and the negative charge on the dummy atom instead on the oxygen. This improves the electrostatic distribution around the water molecule compared to other 3 sites water models.
The dispersion and repulsion forces are defined by the Lennard-Jones potential between the oxygen atoms. Thus the potential is represented by the equation

$$E_{ab} = \sum_i \sum_j \frac{k_c q_i q_j}{r_{ij}} + \frac{A}{r_{OO}^{12}} - \frac{B}{r_{OO}^{6}}. \tag{3.6}$$

An equilibration protocol[71] consisting of 4 individual steps was applied to heat the structure from $0K$ to the desired temperature. This results in an unconstrained well tempered isothermal-isovolume NVT ensemble:

- 50 $ps$ of heating to 165 K using restraints on water molecules (force constant: 1 $kcal\,mol^{-1}$ Å$^{-2}$) with a temperature coupling according to Berendsen[72]
- 50 $ps$ of equilibration $MDS$ at 165 K to temperature coupling according to Andersen[73] including restraints on the molecules.

- 50 $ps$ of equilibration $MDS$ at 165 K to release all restraints using Andersen thermostat
- 50 $ps$ of further heating from 165 K to desired temperature without restraints (Andersen thermostat)

After this procedure a 1 $ns$ equilibration $MDS$ step at constant temperature was carried out to simulate the melting of the ice crystal structure.

As shown in figure 3.10, $MDS$ and $MCRWS$ produce similar shape during simulations: the figure 3.10(a) shows the fourth generation fractal in $MCRWS$ with $U/k_BT = 4.5$ after $10^9$ steps simulation and the figure 3.10(b) the ice crystal during $MDS$ after 620 $ps$ at 270 $K$. At first a net loss of roughness is notable in both cases.

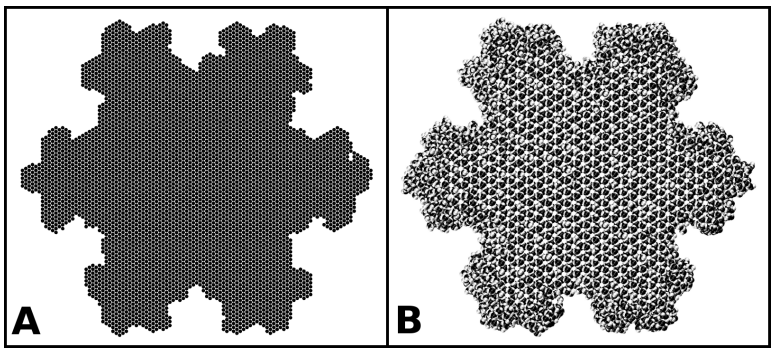


**Figure 3.10: Evolution of filled von Koch-like structures.** (A)Sample of fourth generation during $MCRWS$ after $10^9$ simulation steps with $U/k_BT = 4.5$. (B) Ice crystal during $MDS$ after 620 $ps$ at 270 $K$.

The attention was focused on the observable $\Lambda(t)$, the border length. At time $t = 0$ the perimeter is given by $\Lambda(0) = 3(4^g)l$. $\Lambda(t)$ is connected to the fractal dimension and depends basically on the size of the structure and the roughness of the border. In figure 3.11 the exponential fitting of the border length evolution at two different temperatures for $MDS$ and $MCRWS$ are plotted.

It is remarkable that the decrease of both is very similar. Hence the new model is feasible to reproduce the melting behavior.
The found results for parameterization are:

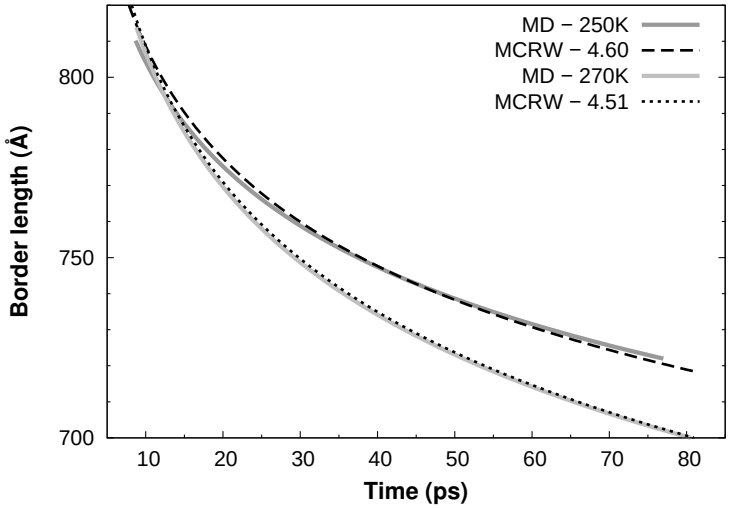


**Figure 3.11: Fit of border length of $3^{rd}$ generation von Koch fractal versus time in seconds.** Comparison between $MCRWS$ and $MDS$ at temperature $T = 270\,K$ (lines below) and temperature $T = 250\,K$ (lines above).

- 1 $ps$ in $MDS$ corresponds to $\approx 16000$ $MCRWS$ steps
- $250K$ and $270K$ in $MDS$ correspond to $U/k_BT$ equal to 4.60 and 4.51 in $MCRWS$, respectively.
- the value of the parameter $U$ found is $\approx 1.6 \times 10^{-20} J$. Notice that in the range $1°C$–$15°C$ the activation free energy for self-diffusion is $4.7 kcal\, mol^{-1}$[74] which implies a value of $U/k_BT$ equal to $\approx 8$.

Afterwards the $MCRWS$ method was employed to simulate higher generations of snowflake fractals, until the $7^{th}$, and analyze carefully the melting process.

## 3.4 Simulations

As the new $MCRWS$ method has much less parameters, variables and equations to compute during the simulation, it is extremely faster than methods with explicit molecules and forces.
The $MCRWS$ can be considered a mesoscopic scale simulation, where the beads represent molecules aggregates of unspecified dimensions.
The algorithm can simulate any shape that lay on a bi-dimensional triangular lattice at this moment. More kinds of lattices can be defined in future.

In figure 3.12 simulation snapshots of collapsing of a $5^{th}$ generation snow-fractal are illustrated. During the melting the loss and re-aggregation of bead clearly generate figures of sequentially lower generations shape, i.e. the tips that characterize the $4^{th}$ (figure 3.12d), and later on the $3^{rd}$ (figure 3.12d), generation are visible in the simulated shapes.

### 3.4.1 Border length

$MCRWS$ was employed to analyze the border length during melting of snowflake fractals of generations $4^{th}$ to $7^{th}$.
Figure 3.13 shows the computed results of the normalized perimeter $\Lambda(t)/\Lambda(0)$ of the flakes during the simulations where the ratio $U/k_BT = 4.2$. The higher the generation, the more regular the decrease. This can be ascribed to some crossover effects that cover the expected fractal features [75, 76].

These curves perform a decrease in the analyzed range given by a double exponential fit:

$$\frac{\Lambda(t)}{\Lambda(0)} = p_g \exp\left(-k_g t\right) + p_{rest} \exp\left(-k_{rest} t\right). \tag{3.7}$$

To find an explanation the the weights of the two exponentials ($p_g$ and $p_{rest}$) were observed. The weight $p_g$ is, in good approximation, the number of the beads that characterize the last fractal generation over the initial (i.e. perfect fractal) perimeter $p_g = 3 \times 4^{g-1}/\Lambda(0) = 0.25$. This "walkers" ensemble has a life time which depends on the factor $U/k_BT$ and on the structure size. It is orders of magnitude larger than that of the rest of the structure $k_{rest}$. That means the two scaling regions can be used to distinguish between two distinct thermal evolution stages. In the first a transition

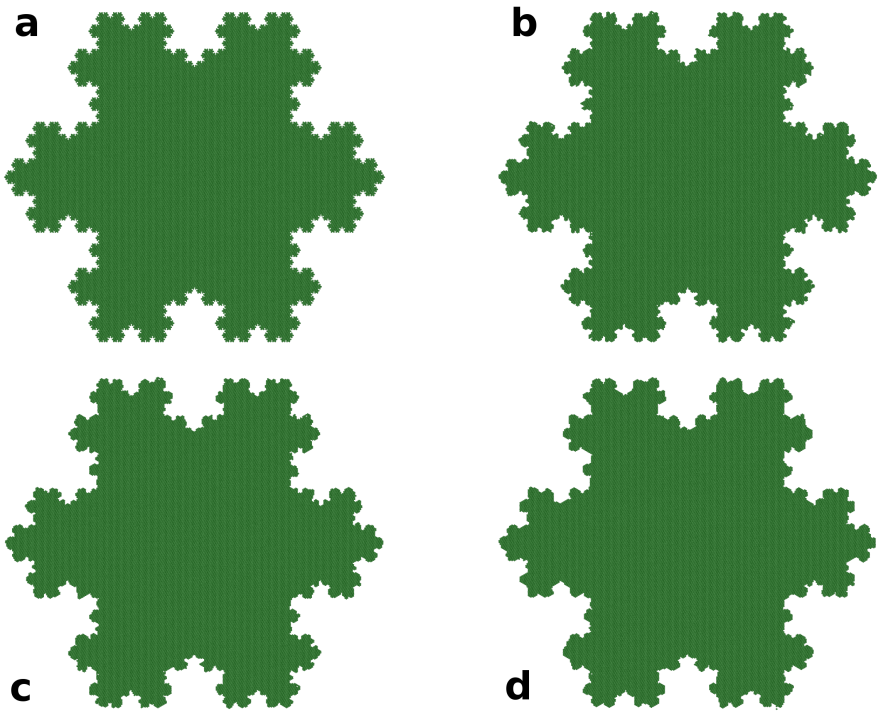


**Figure 3.12:** $MCRWS$ **simulation snapshot of** $5^{th}$ **generation snow-fractal.** Number of simulation steps: (a) 0; (b) $0.125 \times 10^9$; (c) $0.625 \times 10^9$; (d) $2.50 \times 10^9$

from $(g)$ to $(g-1)$ happens and in the second the collapse of the remaining structure is described. In the table 3.1 the coefficients that fits $MCRWS$ data in figure 3.13 are reported:

### 3.4.2 Radius of gyration

Another important observable which was monitored is the radius of gyration of the crystal.

The radius of gyration $R_g$ is defined in polymer physics [77] to be proportional to the root mean square distance, namely

$$R_g = \sqrt{\frac{1}{2N^2}\sum_{i,j}^{N}(r_i - r_j)^2} \tag{3.8}$$

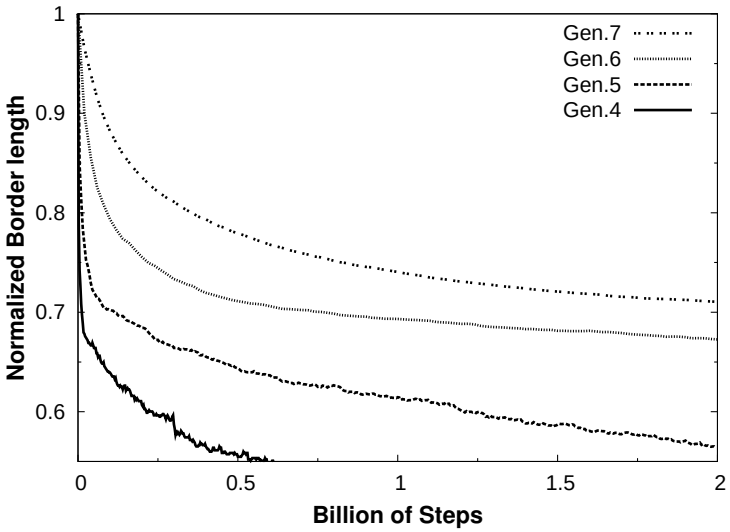


**Figure 3.13: Normalized snowflake border length.** $\Lambda(t)/\Lambda(0)$ from the fourth to seventh initial generation versus time in simulation steps $\times 10^6$.

| Generation | $p_g$ | $p_{rest}$ | $k_g$ | $k_{rest}$ |
|---|---|---|---|---|
| 4 | 0.257 | 0.698 | 0.338 | $1.13 \times 10^{-3}$ |
| 5 | 0.256 | 0.730 | 0.107 | $3.28 \times 10^{-4}$ |
| 6 | 0.242 | 0.725 | 0.0115 | $3.95 \times 10^{-5}$ |
| 7 | 0.231 | 0.728 | 0.00555 | $2.12 \times 10^{-5}$ |

**Table 3.1:** Weights and exponential coefficients of Eq.(3.7) referred to Fig.3.13.

where $N$ is the number of jointed beads at time $t$ and $(r_i - r_j)$ represents the distance, i.e., the minimal path which connects bead $i$ to bead $j$. In order to calculate $R_g$, the formula derived by Rathbeger et al. in [78] was used. The connectivity matrix concept is needed to perform such a calculation[79, 80, 81].

The connectivity matrix $\mathbf{A} = A_{ij}$ is a real symmetric matrix. The diagonal elements $a_{ij}$ are equal to $-1$ if the "walkers" $i$ and $j$ are neighbors and otherwise zero. The diagonal elements are

$$A_{ii} = -\sum_j A_{ij} \tag{3.9}$$

This matrix is being the discrete version of the Laplacian operator and used for many applications; in this case it turns useful in order to get the interbead distances. Following Eq.(14) in [78] it results in:

$$(r_i - r_j)^2 = l^2 \sum_{\alpha=2}^{N} (Q_{i\alpha} - Q_{j\alpha})^2 \lambda_\alpha^{-1}, \tag{3.10}$$

where $l^2$ is the square of the unity lattice length, $Q_{i\alpha}$ are the elements of the eigenvector corresponding to the eigenvalue $\lambda_\alpha$ of $\mathbf{A}$. The sum over $\alpha$ starts from 2 because it was assumed that $\lambda_1$ is the vanishing eigenvalue. By inserting Eq. (3.10) into Eq. (3.8) one obtains

$$R_g^2(t) = \frac{1}{2N^2} \sum_{i,j}^{N} \sum_{\alpha=2}^{N} (Q_{i\alpha} - Q_{j\alpha})^2 \lambda_\alpha^{-1}. \tag{3.11}$$

In figure 3.14 the comparison between the normalized border length $\Lambda(t)/\Lambda(0)$ with the normalized radius of gyration $R_g^2(t)/R_g^2(0)$ versus time for an initial structure of $4^{th}$ generation is shown, i.e. the maximal generation for which a numerical diagonalization of $\mathbf{A}$ could be afford.

Similar to the discussion of figure 3.13, also for $R_g^2(t)/R_g^2(0)$ a double exponential function (see the right hand side of Eq. 3.7) fits the data. However, the weights are now given by the number of beads which characterize the last fractal generation over the initial surface area (total number of beads $N$) $p_g = 3 \times 4^{g-1}/N$ and its complement to one. The best double exponential fit is obtained for the following values: $p_g = 0.04$, $p_{rest} = 0.956$, $k_g = 0.222$, and $k_{rest} = 1.34 \times 10^{-4}$.

Remarkably the exponential coefficients result of the same order of magnitude for both quantities, see the first line of Table 3.1.

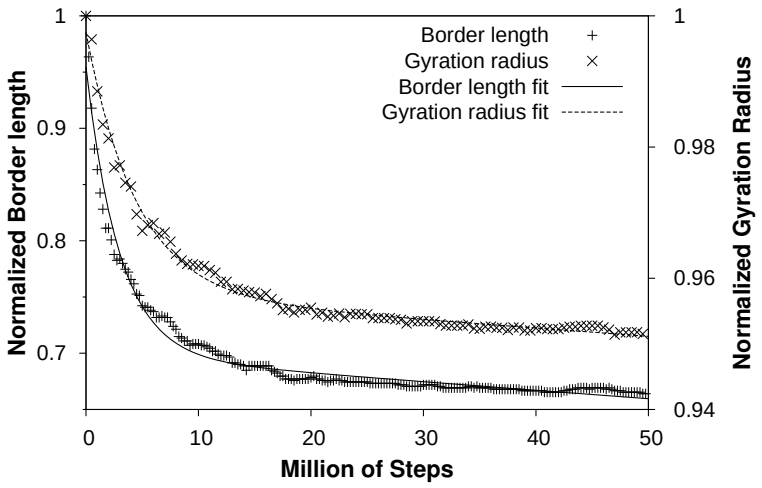


**Figure 3.14: Normalized border length and normalized gyration radius, versus time in arbitrary units.** The effective output of the simulation and its best double exponential fit are plotted.

# 4

# Conclusions

In the present PhD thesis two topics of research in microfluidics were discussed: "Droplet slippage on special surfaces" and "Mesoscopic snowflake melting in terms of fractals".

In the first topic the slippage of a nano-droplet of water adsorbed on a surface with photo-switchable wettability characteristics was studied. A new implicit surface potential was developed to better account for the wettability switch affecting one half of the surface. Application of this new potential within a Molecular Dynamics framework led to successful reproduction of the droplet slippage in direction of the more hydrophilic side of the surface.

Based on this initial results, more detailed analysis was carried out especially with respect to the behaviour of water molecules in direct contact with the surface. Droplet translocation rate was studied under various conditions and conclusions drawn with respect to efficiency. A special role was identified for dipole interactions as well as diffusion taking place in the immediate vicinty of the potential switch.

An interpretation of the microscopic driving force that induces the slippage of the entire drop was proposed. The potential switch could trigger an accumulation of less energetic parallel alignments of dipoles directed towards the "hydrophilic" part of the surface. Such "misaligned" dipoles would then be prone to continued forward-movement to release the "dipole strain" resulting in a re-arrangement of dipoles in the more stable anti-parallell configuration thereby pushing forward the entire core of the drop.

In the second part of this thesis a mesoscopic study was carried out regarding the melting of a snowflake in fractal description.

## 4. CONCLUSIONS

A filled von Koch-like fractal structure of mesoscopic beads was chosen to represent the snowflake. A new algorithm based on Monte Carlo and Random Walk Simulations ($MCRWS$) was developed from scratch to simulate the thermal collapse of fractal structures.

In order to validate the developed method, it was compared with Molecular Dynamics simulations regarding the melting of a snowflake at atomic level of detail. Good agreement could be reached between the two methods and new ice parameters for $MCRWS$ were derived.

The $MCRWS$ method permitted bigger snow-fractals melting studies looking at the time evolution at different temperatures. An in-depth analysis of observables such as border length and gyration radius was performed in order to better describe the melting process.

Both observables showed a decrease during $MCRWS$ simulation which followed the same mathematical law, i.e. a sum of two terms each describing an exponential decay. The two processes were mutually dependent with the initial term decisive for the early drop and the second term dominant in the later stabilization stage of observable trends. Corresponding coefficients and exponentials were determined from the fit to the simulation data.

# References


[1] J. Israelachvili. *Intermolecular & Surface Forces*. Ed. Academic Press, 1991. 1, 30

[2] P. Tabeling. *Introduction to Microfluidics*. Oxford University Press, New York, 2005. 1

[3] J. Israelachvili. **Techniques for direct measurements of forces between surfaces in liquids at the atomic scale**. *Chemtracts-Anal Phys. Chem.*, **1**:1, 1989. 1

[4] J. Koplik and J.R. Banavar. **Continuum Deductions from Molecular Hydrodynamics**. *Annual Review of Fluid Mechanics*, **27**(1):257–292, 1995. Available from: http://www.annualreviews.org/doi/abs/10.1146/annurev.fl.27.010195.001353. 1

[5] B. C. Christner, R. Cai, C. E. Morris, K. S. McCarter, C. M. Foreman, M. L. Skidmore, S. N. Montross, and D. C. Sands. **Geographic, seasonal, and precipitation chemistry influence on the abundance and activity of biological ice nucleators in rain and snow**. *Proc. Natl. Acad. Sci.*, **105**(48):18854–18859, 2008. Available from: http://www.pnas.org/content/105/48/18854.abstract. 2

[6] A. Martini, L. Ferro-Famil, and E. Pottier. **Polarimetric study of scattering from dry snow cover in alpine areas**. In *Geoscience and Remote Sensing Symposium, 2003. IGARSS '03. Proceedings. 2003 IEEE International*, **2**, pages 854–856 vol.2, 2003. 2

[7] H. von Koch. **Sur une courbe continue sans tangente, obtenue par une construction gomtrique lmentaire**. *Archiv fr Matemat., Astron. och Fys.*, **1**:681–702, 1904. 2, 53

[8] J. Berna, D.A. Leigh, M. Lubomska, S.M. Mendoza, E.M. Perez, P. Rudolf, G. Teobaldi, and F. Zerbetto. **Macroscopic transport by synthetic molecular machines**. *Nature Materials*, **4**:704–710, 2005. 3

[9] C. Dietrich-Buchecker and J.P. Sauvage. *Molecular Catenanes, Rotaxanes and Knots: A Journey Through the World of Molecular Topology*. Wiley-VCH, Weinheim, 1999. 3

[10] M. Venturi, A. Credi, and V. Balzani. *Molecular Devices and Machines - A Journey into the Nanoworld*. Wiley-VCH, Weinheim, 2003. 3

[11] E.R. Leigh and D.A. Kay. *Functional Artificial Receptors*. Wiley-VCH, Weinheim, 2005. 3

[12] T.J. Huang. **A nanomechanical device based on linear molecular motors**. *Appl. Phys. Lett.*, **85,**:5391–5393, 2004. Available from: http://dx.doi.org/10.1063/1.1826222. 3

[13] A.H. Flood. **Meccano on the nanoscale - A blueprint for making some of the world's tiniest machines**. *Aust. J. Chem.*, **57,**:301–322, 2004. Available from: http://dx.doi.org/10.1071/CH03307. 3

[14] G. Bottari, D.A. Leigh, and E.M. Perez. **Chiroptical switching in a bistable molecular shuttle**. *J. Am. Chem. Soc.*, **125**:13360–13361, 2003. Available from: http://dx.doi.org/10.1021/ja036665t. 3

[15] D.-H. Qu, Q.-C. Wang, J. Ren, K. Chen, and H. Tian. **A lockable light-driven molecular shuttle with a fluorescent signal**. *Angew. Chem. Int. Edn Engl.*, **43**:2661–2665, 2004. Available from: http://dx.doi.org/10.1002/anie.200453708. 3

[16] D.-H. Qu, Q.-C. Wang, J. Ren, and H. Tian. **A light-driven rotaxane molecular shuttle with dual fluorescence addresses**. *Org. Lett.*, **6**:2085–2088, 2004. 3

[17] E.M. Perez, D.T.F. Dryden, D.A. Leigh, G. Teobaldi, and F. Zerbetto. **A generic basis for some simple light-operated mechanical molecular machines**. *J. Am. Chem. Soc.*, **126**:12210–12211, 2004. 3

[18] D.A. Leigh. **Patterning through controlled submolecular motion: Rotaxane-based switches and logic gates that function in solution and polymer films**. *Angew. Chem. Int. Edn Engl.*, **44**:3062–3067, 2005. Available from: http://dx.doi.org/10.1002/anie.200500101. 3

[19] A. Altieri. **Remarkable positional discrimination in bistable light- and heat-switchable hydrogen-bonded molecular shuttles**. *Angew. Chem. Int. Edn Engl.*, **42**:2296–2300, 2003. Available from: http://dx.doi.org/10.1002/anie.200250745. 3

[20] **Contact angle**. http://en.wikipedia.org/wiki/Contact_angle. Available from: http://en.wikipedia.org/wiki/Contact_angle. 4

[21] S. Singh, J. Houston, F. van Swol, and C. J. Brinker. **Drying transition of confined water**. *Nature*, **442**:526, 2006. 4, 9

[22] Y. Masaaki and M. Masashi. *Newest Aspects of Fluoro Functional Materials*. CMC, Tokyo, 1994. 4

[23] M. Cavallini. **Information storage using supramolecular surface patterns**. *Science*, **299**:531, 2003. Available from: http://dx.doi.org/10.1126/science.1078012. 4

[24] K. Kim. **A pseudorotaxane on gold: Formation of self-assembled monolayers, reversible dethreading and rethreading of the ring, and ion-gating behavior**. *Angew. Chem. Int. Edn Engl.*, **42**:2293–2296, 2003. Available from: http://dx.doi.org/10.1002/anie.200250692. 4

[25] B. Long, K. Nikitin, and D. Fitzmaurice. **Assembly of an electronically switchable rotaxane on the surface of a titanium dioxide nanoparticle**. *J. Am. Chem. Soc.*, **125**:15490–15498, 2003. 4

# REFERENCES


[26] E. Katz, I. Sheeney Haj, and I. Willner. **Electrical contacting of glucose oxidase in a redox-active rotaxane configuration**. *Angew. Chem. Int. Edn Engl.*, **43**:3292–3300, 2004. Available from: http://dx.doi.org/10.1002/anie.200353455. 4

[27] T.J. Huang. **Mechanical shuttling of linear motor-molecules in condensed phases on solid substrates**. *Nano Lett.*, **4**:2065–2071, 2004. Available from: http://dx.doi.org/10.1021/nl035099x. 4

[28] H.-R. Tseng, D. Wu, N.X. Fang, X. Zhang, and J.F. Stoddart. **The metastability of an electrochemically controlled nanoscale machine on gold surfaces**. *Chem. Phys. Chem.*, **5,**:111–116, 2004. 4

[29] S.S. Jang. **Structures and properties of self-assembled monolayers of bistable [2]rotaxanes on Au (111) surfaces from molecular dynamics simulations validated with experiment**. *J. Am. Chem. Soc.*, **127**:1563–1575, 2005. Available from: http://dx.doi.org/10.1021/ja044530x. 4

[30] M.K. Chaudhury and G.M.Whitesides. **How to make water run uphill**. *Science*, **256**:1539–1541, 1992. 6

[31] M.P. Allen and D.J. Tildesley. *Computer Simulation of Liquids*. Oxford U. Press, New York, 1987. 8, 19, 25

[32] A.R. Leach. *Molecular Modelling Principles and Applications 2nd Ed.* Pearson Education, London, 2002. 13

[33] L. Verlet. **Computer "Experiments" on Classical Fluids. I. Thermodynamical Properties of Lennard-Jones Molecules**. *Phys. Rev.*, **158**:98–103, 1967. 18

[34] W.C. Swope, H.C. Anderson, P.H. Berens, and K.R. Wilson. **A computer simulation method for the calculation of equilibrium constants for the formation of physical clusters of molecules: Application to small water clusters**. *J. Chem. Phys.*, **76**:637–649, 1982. 19

[35] D. Beeman. **Some Multistep Methods for Use in Molecular Dynamics Calculations**. *J. Comp. Phys.*, **20**:130–139, 1976. 19

[36] L. V. Woodkock. **Isothermal molecular dynamics calculations for liquid salts**. *Chem. Phys. Lett.*, **10**:257–261, 1971. 20

[37] H. J. C. Berendsen, J.P.M. Postma, W.F. van Gunsteren, A. Di Nola, and J.R. Haak. **Molecular dynamics with coupling to an external bath**. *J. Chem. Phys.*, **81**:3684–3690, 1984. 20

[38] A. Wallqvist and R.D. Mountain. **Molecular models of water: Derivation and description**. *Rev. Comput. Chem.*, **13**:183–247, 1999. 21

[39] W.L. Jorgensen and J. Tirado-Rives. **Chemical Theory and Computation Special Feature: Potential energy functions for atomic-level simulations of water and organic and biomolecular systems**. *Proc. Natl. Acad. Sci.*, **102**:6665–6670, 2005. 21

[40] A. Brodsky. **Is there predictive value in water computer simulations?** *Chem. Phys. Lett.*, **261**:563–568, 1996. 22

[41] B.Guillot. **A reappraisal of what we have learnt during three decades of computer simulations on water**. *J. Mol. Liquids*, **101**:219–260, 2002. 22

[42] H.J.C. Berendsen, J.P.M. Postma, W.F. van Gunsteren, and J. Hermans. *Intermolecular Forces*. B. Pullman (Reidel, Dordrecht), 1981. 23

[43] H.J.C. Berendsen, J.R. Grigera, and T.P. Straatsma. **The missing term in effective pair potentials**. *J. Phys. Chem.*, **91**:6269–6271, 1987. 23

[44] J. C. Phillips, R. Braun, W. Wang, J. Gumbarta, E. Tajkhorshid, E. Villa, C. Chipot, R. D. Skeel, L. Kale, , and K. Schulten. **Scalable molecular dynamics with NAMD**. *J. Comp. Chem.*, **26**:1781–1802, 2005. 25

[45] B. R. Brooks, R. E. Bruccoleri, B. D. Olafson, D. J. States, S. Swaminathan, and M. Karplus. **CHARMM: a program for macromolecular energy, minimization, and dynamics calculations**. *J. Comp. Chem.*, **4**(2):187–217, 1983. 25

[46] A. T. Brünger. *X-PLOR, Version 3.1, A System for X-ray Crystallography and NMR*. The Howard Hughes Medical Institute and Department of Molecular Biophysics and Biochemistry, Yale University, 1992. 25

[47] F. C. Bernstein, T. F. Koetzle, G. J. B. Williams, J. E. F. Meyer, M. D. Brice, J. R. Rodgers, O. Kennard, T. Shimanouchi, and M. Tasumi. **The protein data bank: A computer-based archival file for macromolecular structures**. *J. Mol. Biol.*, **112**:535–542, 1977. 26

[48] W. Humphrey, A. Dalke, and K. Schulten. **VMD - Visual Molecular Dynamics**. *J. Molec. Graphics*, **14**(1):33–38, 1996. 27, 28

[49] A. Rahman and F. H. Stillincer. **Molecular dynamic study of liquid water**. *J. Chem. Phys.*, **55**(7):3356–3359, 2001. 28

[50] T. Cramer, F. Zerbetto, and R. García. **Molecular Mechanism of Water Bridge Buildup: Field-Induced Formation of Nanoscale Menisci**. *Langmuir*, **24**:6116–6120, 2008. 31

[51] M. Abramowitz and I. A. Stegun. *Handbook of Mathematical Functions*. Dover Publications, 1965. 33

[52] F. Lugli and F. Zerbetto. **Molecular Dynamics of Nanobubbles Collapse in Ionic Solutions**. *ChemPhysChem*, **8**(1):47–49, 2007. Available from: http://dx.doi.org/10.1002/cphc.200600412. 47

[53] R.W. Impey, P.A. Madden, and I.R. McDonald. **Hydration and mobility of ions in solution**. *J. Phys. Chem.*, **87**:5071–5083, 1983. 47

[54] F.W. Starr, J.K. Nielsen, and H.E. Stanley. **Hydrogen-bond dynamics for the extended simple point-charge model of water**. *Phys. Rev. E*, **62**(1):579–587, Jul 2000. 48

[55] R. Kumar, J.R. Schmidt, and J.L. Skinner. **Hydrogen bonding definitions and dynamics in liquid water**. *The Journal of Chemical Physics*, **126**(20):204107, 2007. Available from: http://link.aip.org/link/?JCP/126/204107/1. 48

[56] A. Einstein. **Über die von der molekularkinetischen Theorie der Wärme geforderte Bewegung von in ruhenden Flüssigkeiten suspendierten Teilchen**. *Ann. Physik*, **17**:549–559, 1905. [translated as Chapter I in Einstein (1926/56)]. 49

[57] A. Einstein. **Zur Theorie der Brownschen Bewegung**. *Ann. Physik*, **19**:371–381, 1906. [translated as Chapter II in Einstein (1926/56)]. 49

[58] A. Einstein. *Investigations on the Theory of the Brownian Movement*. Methuen, London, 1926. [Dover, New York (2nd ed., 1956)]. 49, 55

[59] M. Smoluchowski. **Zur kinetischen Theorie der Brownschen Molekularbewegung und der Suspensionen**. *Ann. Physik*, **21**:756–780, 1906. 49, 55

[60] M. Smoluchowski. **Drei Vorträge über Diffusion, Brownschen Bewegung und Koagulation von Kolloidteilchen**. *Physikalische Zeitschrift*, **17**:557–571 and 587–599, 1916. 49

[61] **Fractal dimension**. http://en.wikipedia.org/wiki/Fractal_dimension. Available from: http://en.wikipedia.org/wiki/Fractal_dimension. 54

[62] M. Bigerelle and A. Iost. **Perimeter analysis of the Von Koch island, application to the evolution of grain boundaries during heating**. *J. Mater. Sci.*, **41**:2509–2516, 2006. 54

[63] K.G. Libbrecht. **The physics of snow crystals**. *Rep. Prog. Phys.*, **68**:855, 2005. 54

[64] J. Dai, W. D. Seider, and T. Sinno. **Coarse-grained lattice kinetic Monte Carlo simulation of systems of strongly interacting particles**. *JOURNAL OF CHEMICAL PHYSICS*, **128**(19), MAY 12 2008. 54

[65] M. N. Barber and B. W. Ninham. *Random and Restricted Walks: Theory and Applications*. New York: Gordon and Breach, 1970. 54

[66] G. Polya. **Ueber eine Aufgabe der Wahrscheinlichkeitsrechnung betreffend die Irrfahrt im Strassennetz**. *Math. Ann.*, **84**:149–160, 1921. 55

[67] E.W. Montroll and G.H. Weiss. **Random Walks on Lattices. II**. *Journal of Mathematical Physics*, **6**(2):167–181, 1965. Available from: http://link.aip.org/link/?JMP/6/167/1. 55

[68] E.W. Montroll. In *Proc. Symp. Appl. Mah. Am. Math. Soc.*, **16**, page 193, 1964. 55

[69] D. A. Case et al. **Amber biomolecular simulation programs**. *J. Comput. Chem.*, **26**:1668–1688, 2005. 62

[70] J. L. F. Abascal, E. Sanz, R. Garcia Fernandez, and C. Vega. **A potential model for the study of ices and amorphous water: TIP4P/Ice**. *The Journal of Chemical Physics*, **122**(23):234511, 2005. Available from: http://link.aip.org/link/?JCP/122/234511/1. 62

[71] **based on the equilibration protocol developed by Siegfried Höfinger**. 63

[72] W. F. van Gunsteren and H. J. C. Berendsen. **Algorithms for macromolecular dynamics and constraint dynamics**. *Mol. Phys.*, **34**:1311–1327, 1977. 63

[73] H. C. Andersen. **Molecular dynamics simulations at constant pressure and/or temperature**. *J. Chem. Phys.*, **72**:2384–2393, 1980. 63

[74] R. Mills. **Self-diffusion in normal and heavy water in the range 1–45°C**. *J. Phys. Chem.*, **77**:685–688, 1973. 65

[75] P. Meakin. **Formation of Fractal Clusters and Networks by Irreversible Diffusion-Limited Aggregation**. *Phys. Rev. Lett.*, **51**(13):1119–1122, Sep 1983. 66

[76] P. Meakin. *Fractals, scaling and growth far from equilibrium*. Cambridge Univerity Press, 1998. 66

[77] M. Doi and S. F. Edwards. *The Theory of Polymer Dynamics*. Clarendon, Oxford, 1986. 67

[78] S. Rathgeber, M. Monkenbush, J.L. Hendrik, M. Trollsås, and A.P. Gast. **Starlike dendrimers in solutions: Structural properties and internal dynamics**. *J. Chem. Phys.*, **125**:204908, 2006. 68, 69

[79] O. Mülken, A. Blumen, T. Amtor, Ch. Giese, M. Reetz-Lamour, and M. Weidem. **Survival Probabilities in Coherent Exciton Transfer with Trapping**. *Phys. Rev. Lett.*, **99**:090601, 2007. 68

[80] A. Blumen, Ch. von Ferber, A. Jurjiu, and Th. Koslowski. **Generalized Vicsek Fractals: Regular Hyperbranched Polymers**. *Macromolecules*, **37**:638, 2004. 68

[81] P. Biswas, R. Kant, and A. Blumen. **Stretch dynamics of flexible dendritic polymers in solution**. *J. Chem. Phys.*, **114**:2430, 2001. 68